Electronic Supplementary Information (ESI) for

A Cyclic Trinuclear Silver Complex for Photosynthesis of Hydrogen Peroxide

Ri-Qin Xia,[a] Zhen-Na Liu,[a] Yu-Ying Tang,[a] Xiao Luo,[a] Rong-Jia Wei,[a] Tao Wu,[a] Guo-Hong Ning*[a] and Dan Li*[a]

[a]College of Chemistry and Materials Science, and Guangdong Provincial Key Laboratory of Functional Supramolecular Coordination Materials and Applications, Jinan University, Guangzhou 510632, People's Republic of China

E-mail addresses:
guohongning@jnu.edu.cn (G.-H. Ning)
danli@jnu.edu.cn (D. Li)

Contents

Section S1. Materials and Methods

1.1 Materials. Starting materials, reagents, and solvents were purchased from commercial sources and used without further purification.

1.2 Characterizations and instruments. Powder X-ray diffraction (PXRD) data were collected at 40 kV, 30 mA using microcrystalline samples on a Rigaku Ultima IV diffractometer using Cu-Kα radiation (λ = 1.5418 Å). The measurement parameters include a scan speed of 0.5 °/min, a step size of 0.02°, and a scan range of 2θ from 3° to 40°. Thermogravimetric analysis was performed on a Mettler-Toledo (TGA/DSC1) thermal analyzer. Measurement was made on approximately 5 mg of dried samples under an N_2 flow with a heating rate of 10 °C/min. Fourier transform infrared (FT-IR) spectrum was measured using a Nicolet Avatar 360 FT-IR spectrophotometer. X-ray photoelectron (XPS) spectroscopy spectra were performed by a Thermo ESCALAB 250XI system. Liquid ^1H and ^{13}C NMR spectra were recorded on Bruker Biospin Avance (400 MHz) equipment using tetramethylsilane (TMS) as an internal standard. UV-visible absorption spectra were recorded on Agilent Cary 4000. Energy dispersive X-ray spectroscopy (EDS) analyses were taken on the COXEM EM-30 PLUS System. Electron paramagnetic resonance (EPR) signals were recorded on a Bruker Magnettech ESR 5000 spectrometer (Germany) at room temperature under visible-light irradiation using a 300 W Xenon lamp (>420 nm). The electrochemical measurements were performed in a conventional three-electrode cell on a CHI-760E electrochemical workstation (Shanghai Chenhua Instrument Co., Ltd, China). The apparent quantum yield (AQY) was measured by multi-channel photoreaction system 4-HZJ (Beijing Perfect Light Technology Co., LTD., Beijing, China, PCX50C) and optical radiometer (Beijing Normal University Photoelectric Instrument Factory, PL-MW2000). In-situ Fourier transforms infrared spectrometry was carried out on the Thermo Nicolet iS50 instrument. The sample was filled into an in-situ IR cell, and O_2 and H_2O vapors (The gas flow is 20 mL/min) were introduced into the cell and fiber source (The light intensity is 300 mW/cm^2). The baseline was obtained before the sample reached O_2 adsorption equilibrium within 1 h. Photoluminescence Spectroscopy was performed on the F-7000 FL Spectrophotometer. GC-MS analysis was carried out on an Agilent 7890B GC analyzer. The headspace was sampled continuously (100 μL sample volume) by online gas chromatography (Fuli, GC-9790II) equipped with a thermal conductivity detector (TCD) referencing against standard gas with a known concentration of O_2.

1.2.1 Photoelectrochemical measurement. All electrochemical measurements (photocurrent, Mott Schottky, and EIS) were made in 0.5 M sodium sulfate solution (pH=6.8) through the traditional three-electrode system in the CHI 760E electrochemical workstation. During the photocurrent measurement, an Ag/AgCl electrode was used as the reference electrode and a Pt foil electrode acted as the counter

electrode. The working electrodes were designed using resulting samples covered on the surface of fluoride tin oxide (FTO) conductor glass. A quartz cell filled with 0.5 M Na_2SO_4 (pH=6.8) electrolyte was used as the measurement system. For electrochemical simpedance spectroscopy (EIS) measurements, the amplitude of the sinusoidal wave was 5 mV, and the frequency ranged from 100 kHz to 0.05 Hz.

1.2.2 Photocatalytic reaction. In a typical experiment, the photosynthesis of H_2O_2 was performed in a 10 mL quartz reaction tube containing 4 mg photocatalyst, and 5 mL deionized water was sonicated in the dark for 30 minutes and oxygen bubbles for 15 minutes. Then, the system was irradiated with a xenon lamp source (CEL-HXF300), the light intensity is 0.2739 W/cm^2.The H_2O_2 content in the solution was detected after the catalyst was filtered. The photocatalyst was not damaged after catalysis, as was confirmed by the Inductively coupled plasma mass spectrometry (ICP-MS) of the reaction supernatant.

1.2.3 H_2O_2 detection method. The amount of H_2O_2 was analyzed by iodometry.[1] Taken 1 mL of filtered filtrate and dilute to 10 mL, removed 2 mL then added 1 mL of 0.4 $mol \cdot L^{-1}$ potassium iodide (KI) aqueous solution and 1 mL of 0.1 $mol \cdot L^{-1}$ potassium hydrogen phthalate ($C_8H_5KO_4$) aqueous solution to obtained mixture solution, which was then kept for 12 h. A redox reaction occurs between H_2O_2 molecules and iodine ions (I^-) under acidic conditions to generate triiodide ions (I_3^-), which have strong absorption at about 350 nm. The absorbance of I_3^- at 350 nm is measured by UV-visible absorption spectra (Agilent Cary 4000), and then the amount of H_2O_2 generated by each reaction can be calculated by comparison with the standard curve of H_2O_2.

1.2.4 Rotating disk electrode (RDE) measurements. A glassy carbon rotating disk electrode (Hardware User's Manual Model 636 Electrode Rotator) served as the substrate for working electrode. The working electrode was prepared as followed:**1** (4 mg) was dispersed in EtOH (2 mL) containing Nafion (50 µL) by ultrasonication. The slurry (20 µL) was put onto the disk electrode and dried at room temperature. The linear sweep voltammograms (LSV) were obtained in an O_2-saturated 0.1 M phosphate buffer solution (pH = 7) at room temperature with a scan rate 10 mV s^{-1} and different rotation speeds after O_2 bubbling for 1 hour. During the reaction, light source from the Xe-lamp vertically illuminated at the rotating electrode, where the photoelectrochemical kinetic information and the formation of peroxide could be obtained. The average number of electrons (n) was calculated by Koutecky-Levich equation:

$$\frac{1}{J} = \frac{1}{J_L} + \frac{1}{J_K} = \frac{1}{B\omega^{1/2}} + \frac{1}{J_K}$$

$$B = 0.62nFC_0D_0^{2/3}v^{-1/6}$$

where J is the measured current density, J_K and J_L are the kinetic and diffusion-limiting current densities, ω is the angular velocity, n is transferred electron number, F is Faraday constant (96485 C mol^{-1}), C_0 is the bulk concentration of O_2 (1.26 $\times 10^{-6}$ mol

cm^{-3}), D_0 is the diffusion coefficient of O_2 in 0.1 M phosphate buffer solution (2.7×10^{-5} cm^2 s^{-1}), and v is kinetic viscosity of the electrolyte (0.01 cm^2 s^{-1}), respectively.

1.2.5 The AQY measurement. The photocatalytic reaction was performed in pure deionized water (5 mL) and photocatalyst (4 mg) in a 50 mL photocatalytic reactor. After sonication for 30 min and O_2 bubbling for 15 min, the bottle was irradiated by a multi-channel photoreaction system 4-HZJ (Beijing Perfect Light Technology Co., LTD., Beijing, China, PCX50C). The apparent quantum yield (AQY) of the photocatalyst was measured with 420 nm, 450 nm, 485 nm, 520 nm, and 535 nm band-pass filters. The active area of the reactor is about 6.33 cm^2. Use an optical radiometer to take the average value of monochromatic light intensity at three representative points. Therefore, the light intensity at 420 nm, 450 nm, 485 nm, 520 nm, and 535 nm is calculated as 0.1316 W cm^{-2}, 0.1342 W cm^{-2}, 0.0790 W cm^{-2}, 0.0382 W cm^{-2}, 0.0240 W cm^{-2}, respectively. AQY is calculated as follows[2]:

$$AQY\% = \frac{n_{H2O2} \times 2 \times N_A}{\Delta P \times S \times t \times \dfrac{\lambda}{hc}} \times 100\%$$

n = number of produced H_2O_2 molecules (mol)
N_A (Avogadro constant) = 6.02×10^{23} mol^{-1}
ΔP = the intensity difference of irradiation light (W / cm^2) = 0.1342 W / cm^2 (450 nm)
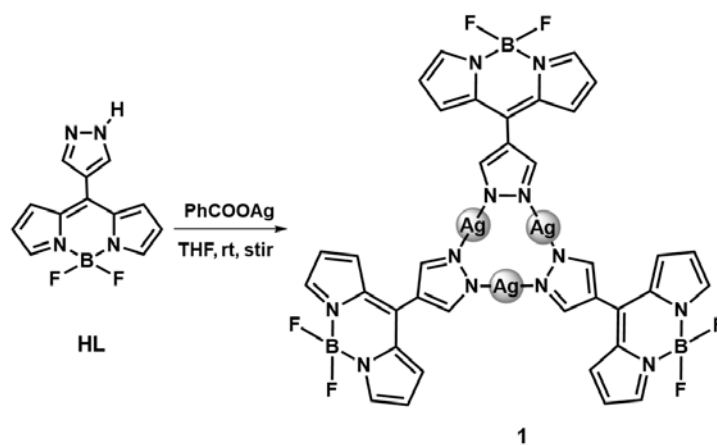S = Irradiation area (cm^2) = 6.33 cm^2
t = the photoreaction time (s) = 3600 s
λ = the wavelength of the monochromatic light (m) = 450×10^{-9} m
h (Planck constant) = 6.626×10^{-34} J·s
c (Speed of light) = 3×10^8 m·s^{-1}

Section S2. Synthesis and Characterizations

Scheme S1 The synthesis of Ag-CTC **1**

Synthesis of 1: HL was synthesized by referring to the reported method[3]. Anhydrous tetrahydrofuran (THF) solution of ligand **HL** (25.8 mg, 0.1 mmol) and PhCOOAg (23 mg, 0.1 mmol) was stirred at room temperature for 24 hours under dark to give the Ag-CTC **1** as orange powder (16.4 mg, Yield: 45% based on HL). ^{1}H NMR (400 MHz, DMSO-d_6, 298 K): δ (ppm) 8.35 (s, 1H), 7.99 (s, 1H), 7.43 (s, 1H), 6.69 (s, 1H). ^{19}F NMR (400 MHz, DMSO-d_6, 298 K): δ (ppm) 141.66 – 141.89 (m). ^{13}C NMR (400 MHz, DMSO-d6, 298 K): δ (ppm) 144.57, 141.92, 141.15, 133.17, 129.98, 118.42, 114.26, 67.49, 49.07, 25.59. Elemental analysis (CHN), $C_{36}H_{24}Ag_3B_3F_6N_{12}(H_2O)_3(CH_3OH)$, calculated (%): C 37.64, H 2.90, N 14.23; found (%): C 37.72, H 2.75, N 13.81.

The crystals of **1** that are suitable for single crystals X-ray diffraction were obtained by solvothermal synthesis. Specifically, **HL** (5.0 mg, 0.02 mmol) and $AgNO_3$ (3.6 mg, 0.02 mmol) were mixed in anhydrous EtOH (2 mL) at 80 ℃ for three days to give **1** as orange crystals, (1.0 mg, Yield: 13.7% based on **HL**).

2.1 NMR spectroscopy.
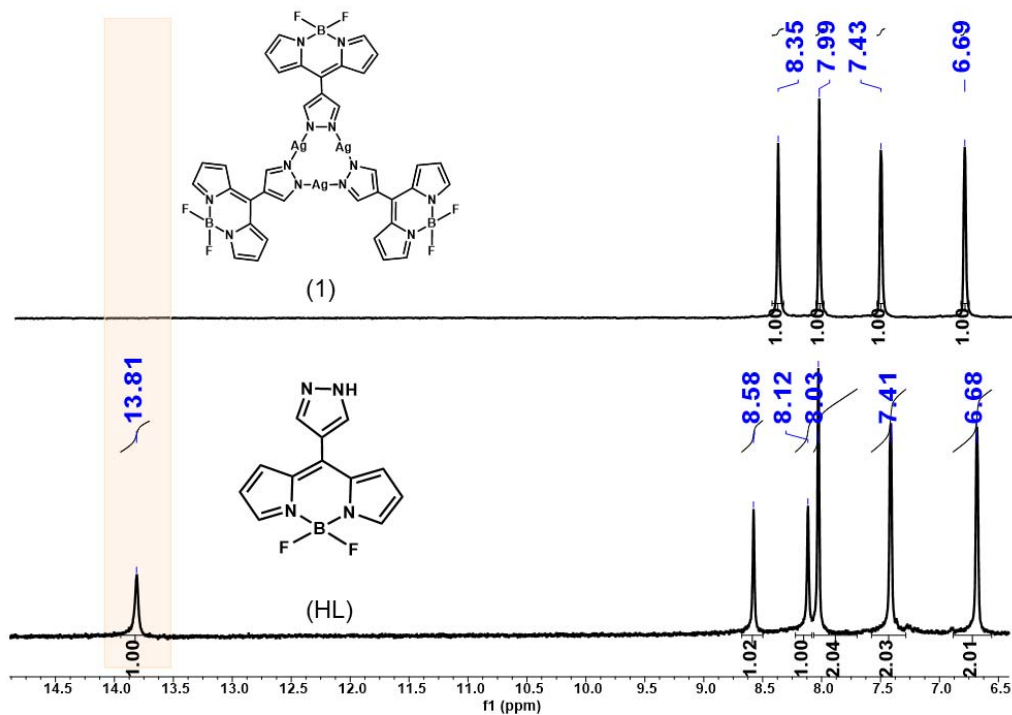
Fig. S1 ^{1}H NMR spectra (400 MHz, DMSO-d_6, 298 K) of **HL** (bottom) and **1** (top).
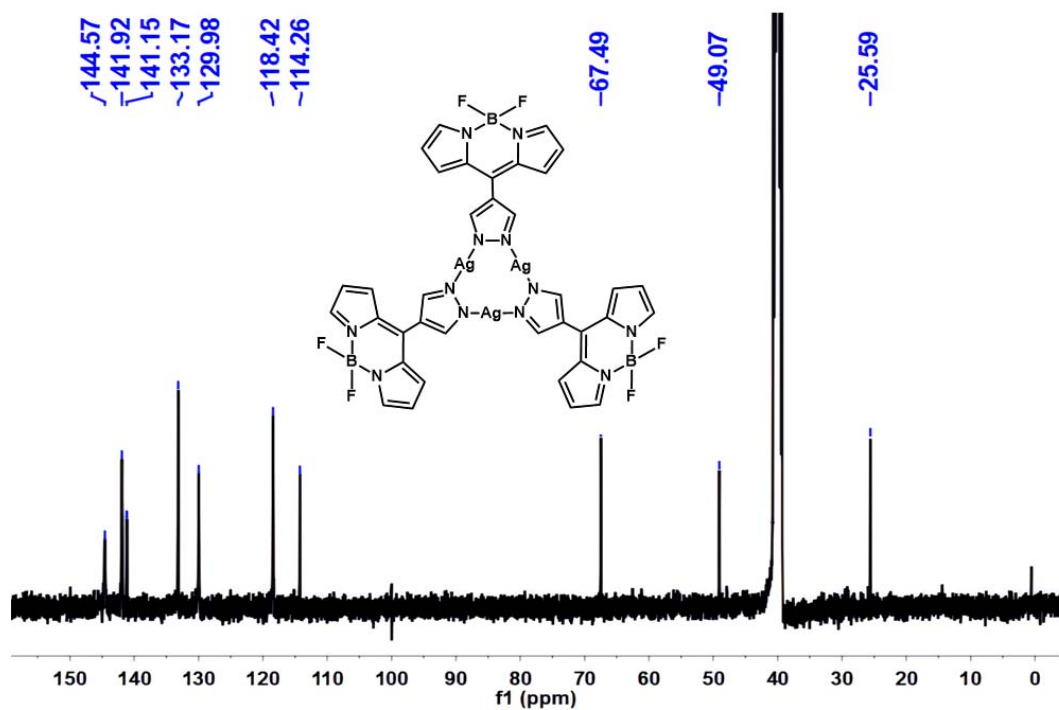
Fig. S2 ^{13}C NMR spectrum (400 MHz, DMSO-d_6, 298 K) of **1**.
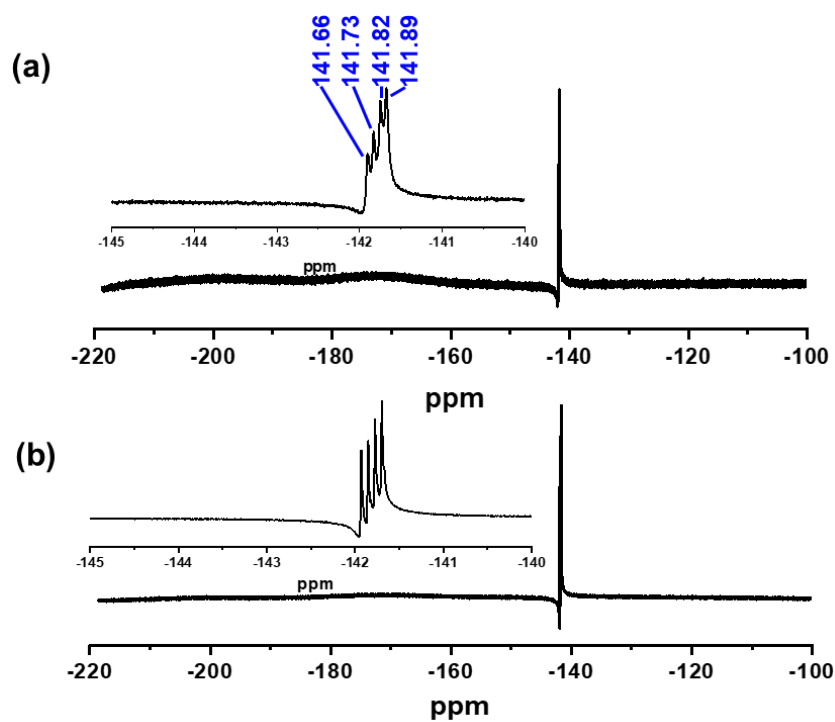
Fig. S3 ^{19}F NMR spectra (400 MHz, DMSO-d_6, 298 K) of (a) **1** and (b) **HL**.

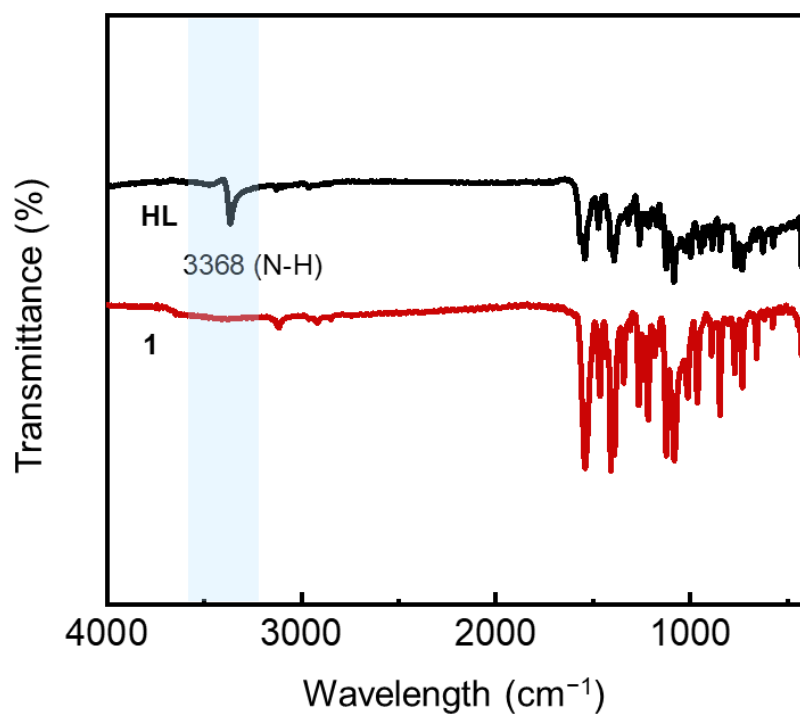## 2.2 Fourier transform infrared spectrum

Fig. S4 FT-IR spectra of **HL** (black line) and **1** (red line).
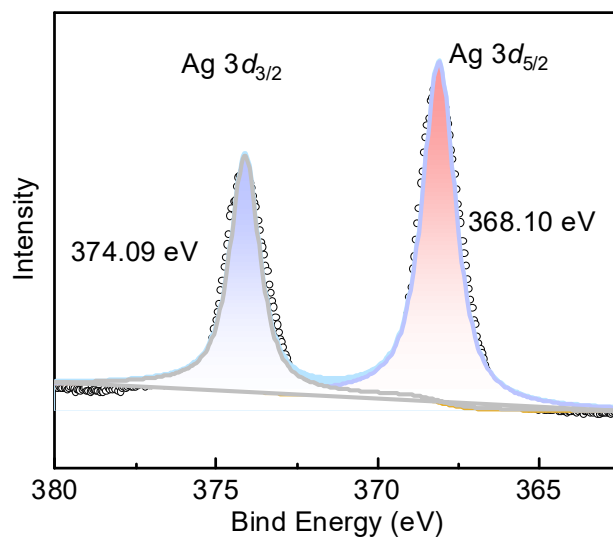
2.3 X-ray photoelectron spectroscopy

Fig. S5 XPS of **1** suggesting all Ag ions are +1.

2.4 Energy dispersive X-ray spectroscopy (EDS)
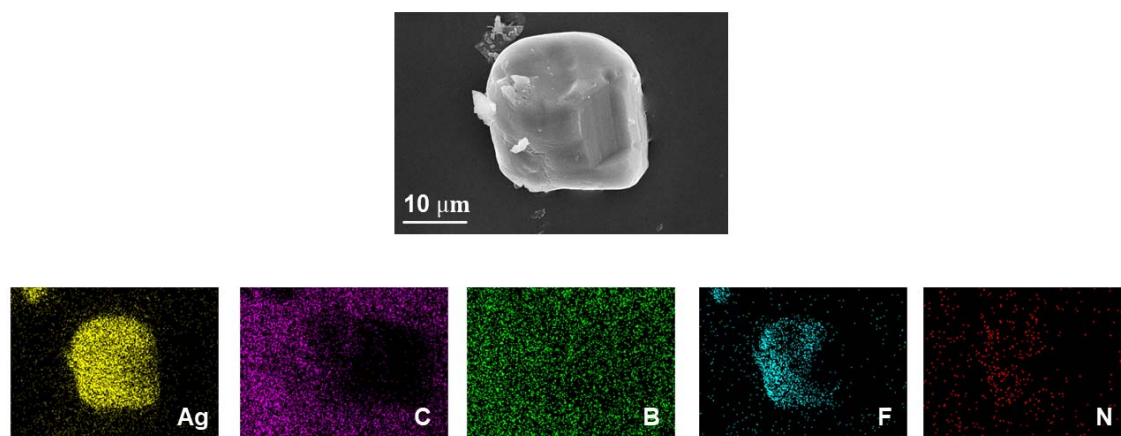
Fig. S6 EDS of **1** showing the uniform distribution of elements Ag, C, B, F and N.
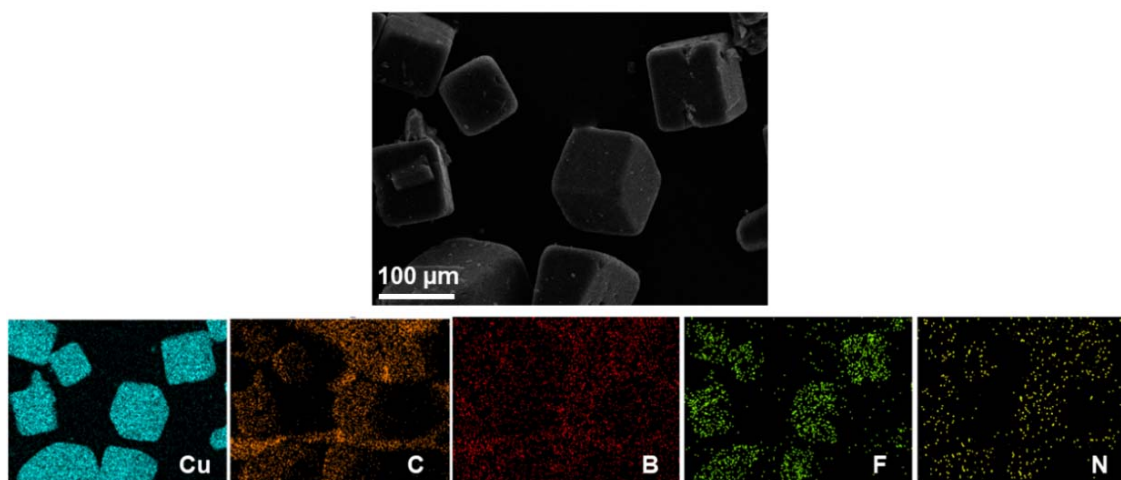
Fig. S7 EDS of **2** showing the uniform distribution of elements Cu, C, B, F and N.
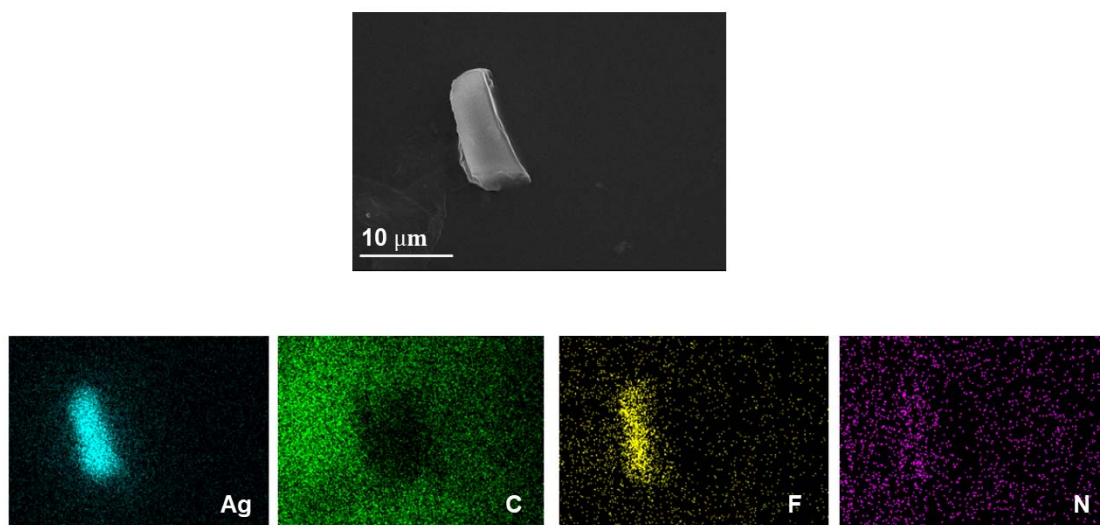
Fig. S8 EDS of **3** showing the uniform distribution of elements Ag, C, F and N.

2.5 Thermogravimetric analysis (TGA)
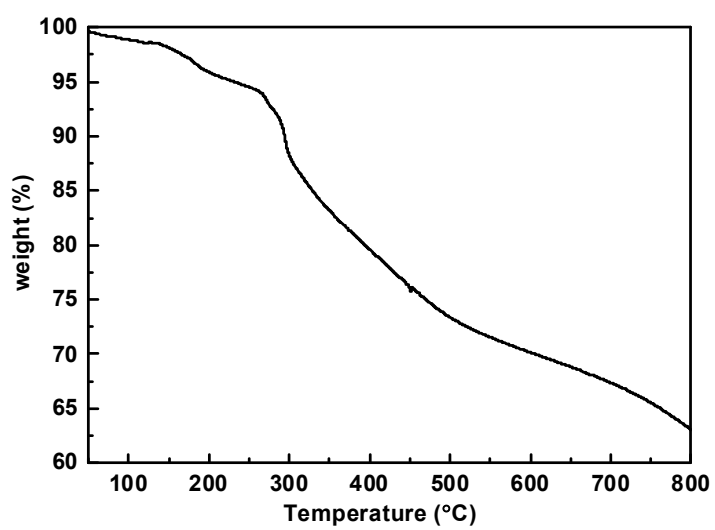
Fig. S9 TGA profile of **1** under N2 atmosphere.

2.6 Power X-ray diffraction (PXRD)
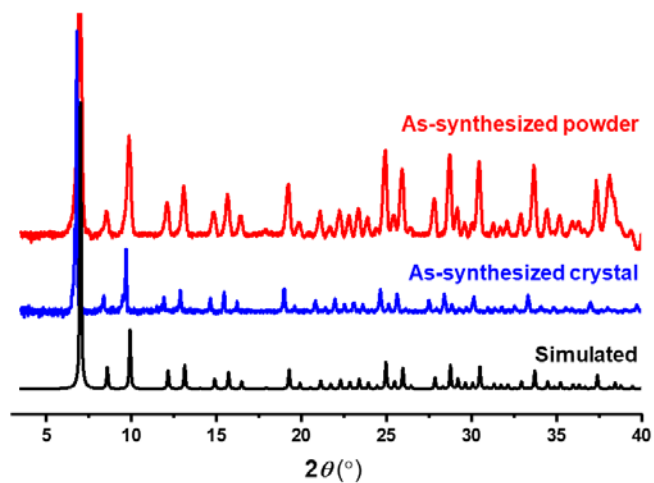
Fig. S10 The comparison of PXRD patterns of simulated (black line), as-synthesized crystals (blue line) and powder (red line) samples of **1**.
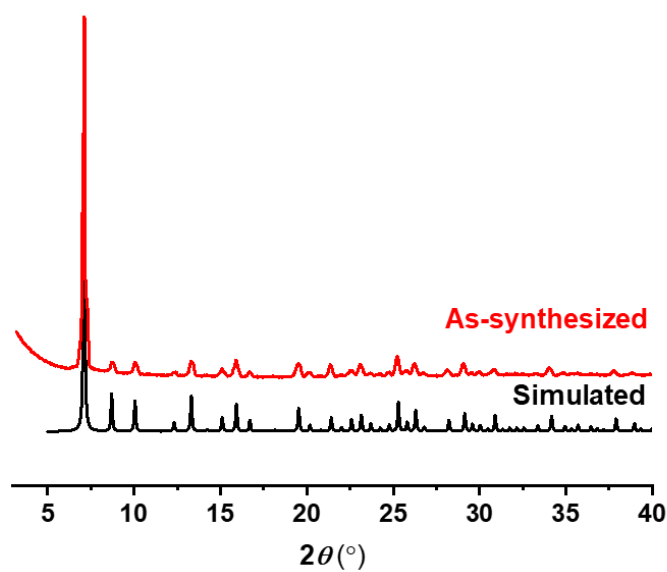
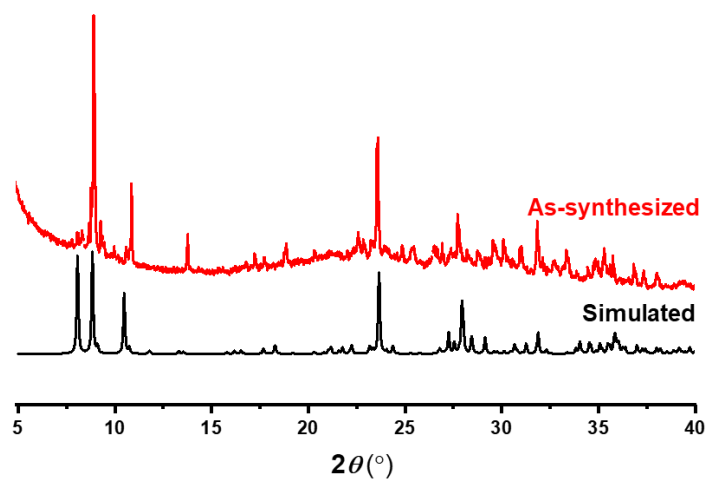**Fig. S11** The comparison of PXRD patterns of simulated and as-synthesized crystal samples of **2**.

Fig. S12. The comparison of PXRD patterns of simulated and as-synthesized crystal samples of **3**.
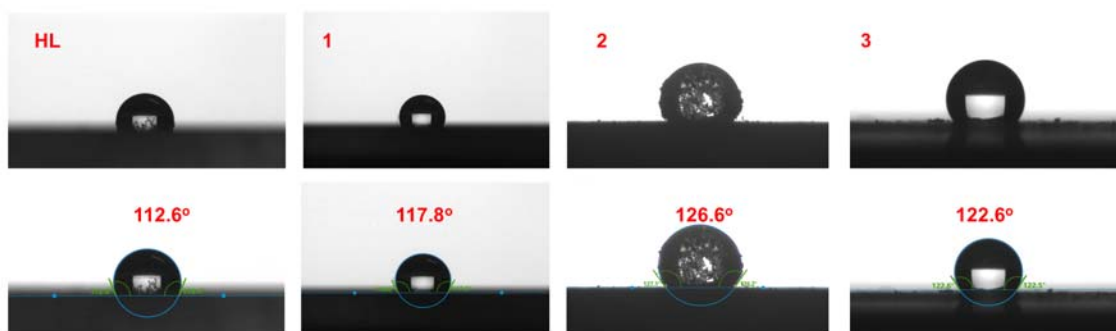
2.7 Measurement of water contact angle

Fig. S13 Water contact angle of **HL**, **1**, **2** and **3**.

2.8 Crystals structure analysis

Suitable single crystal of **1** was mounted with nylon loops. Data was collected on an Oxford Diffraction XtalAB [Rigaku(Cu) Xray dual wavelength source, Kα, λ = 1.5418 Å] equipped with a monochromator and CCD plate detector (CrysAlisPro CCD, Oxford Diffraction Ltd) at 100 K. Single-crystal structures of compound **1** were solved by direct methods by ShelXS[4] in Olex2 1.5[5]. All non-hydrogen atoms were refined with anisotropic thermal parameters, and all hydrogen atoms were included in calculated positions and refined with isotropic thermal parameters riding on those of the parent atoms. Crystal data and structure refinement parameters were summarized in Table S1.
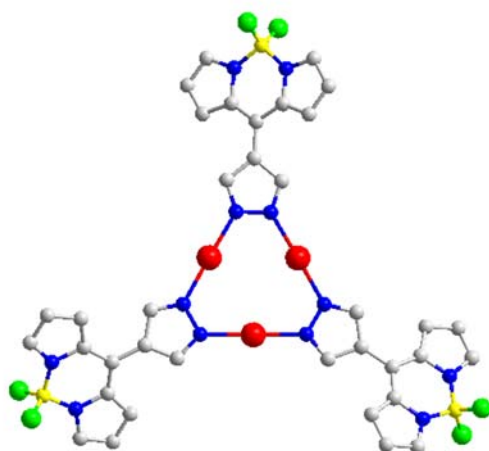

Fig. S14 Structure diagram of **1**. Color codes: N, blue; Ag, red; B, light yellow; and F, light green. H atoms are omitted for clarity.
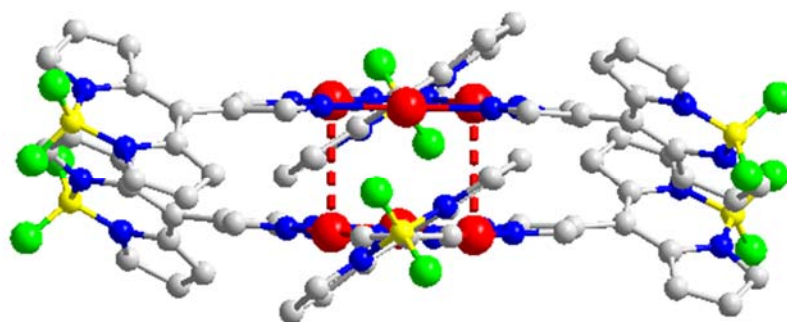

Fig. S15 Stacked diagram showing a dimer of compound **1**, and the distance between Ag···Ag is 3.75 Å. Color codes: N, blue; Ag, red; B, light yellow; and F, light green. H atoms are omitted for clarity.

Table S1 Crystal system, space group, and unit cell parameters of **1**.

Parameter	1
Empirical formula	$C_{12}H_8AgBF_2N_4$
Formula weight	364.90
Temperature (K)	100.00(11)
Wavelength (Å)	1.54178
Crystal system	cubic
Space group	*Ia-3*
a (Å)	25.1961(3)
b (Å)	25.1961(3)
c (Å)	25.1961(3)
α (°)	90
β (°)	90
γ (°)	90
Volume (Å^3)	15995.6(6)
Z	48
ρ_{calc} g / cm^3	1.818
μ / mm^{-1}	12.307
F(000)	8544.0
2θ range for data collection (°)	4.2740 to 77.0860
Index ranges	$-31 \le h \le 31$ $-31 \le k \le 29$ $-31 \le l \le 25$
Reflections collected	2849
Independent reflections	2156 [R_{int} = 0.0865, R_{sigma} = 0.140]
Completeness (%)	100
Data / restraints / parameters	2849 / 0 / 181
Largest diff. peak and hole (e/Å^3)	1.821, −0.575
Goodness-of-fit on F^2	1.089
R_1[a] [I>=2sigma(I)]	0.0676
wR_2[b] (all data)	0.2250
DOI	10.5517/ccdc.csd.cc2gqh2s

[a]$R_1 = \Sigma|F_o| - |F_c||/\Sigma|F_o|$. [b]$wR_2 = \{[\Sigma w(F_o^2 - F_c^2)^2]/\Sigma[w(F_o^2)^2]\}^{1/2}$; w = 1/ [$\sigma^2(F_o^2) + (aP)^2 + bP$], where $P = [\max(F_o^2,0) + 2F_c^2]/3$ for all data.
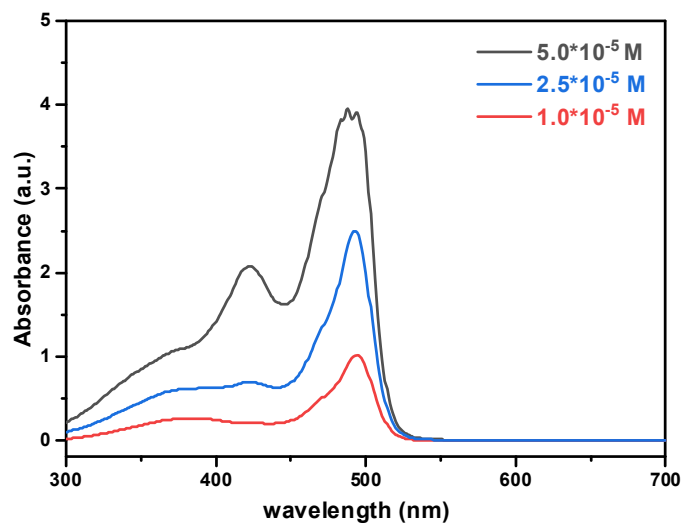
2.9 UV-Vis spectra

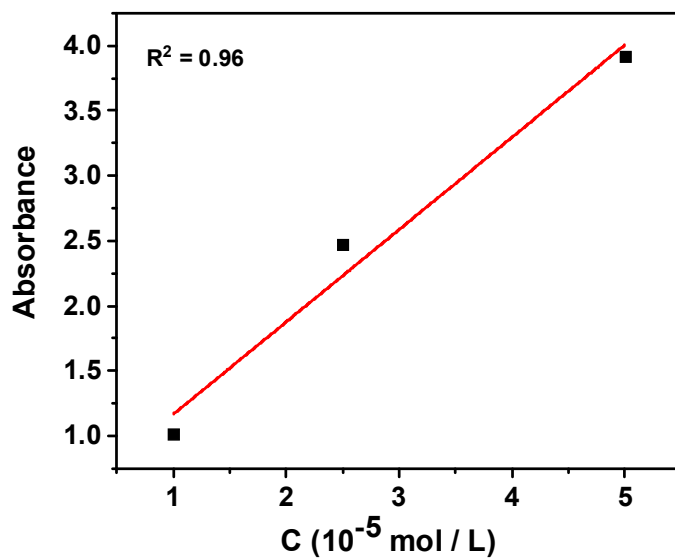**Fig. S16** UV-Vis spectra of **1** in DMSO.

Fig. S17 Absorbance-concentration fitting curve of **1**. R^2 = 0.96.
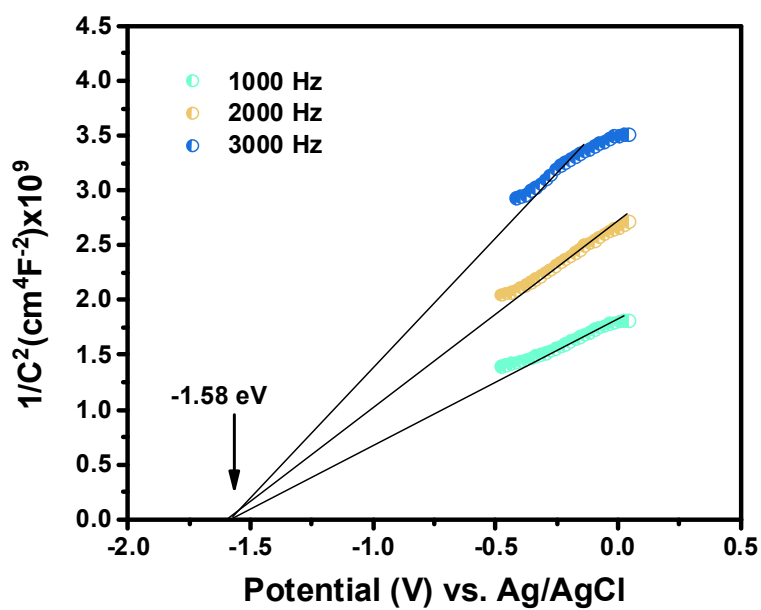
2.10 Mott-Schottky plot
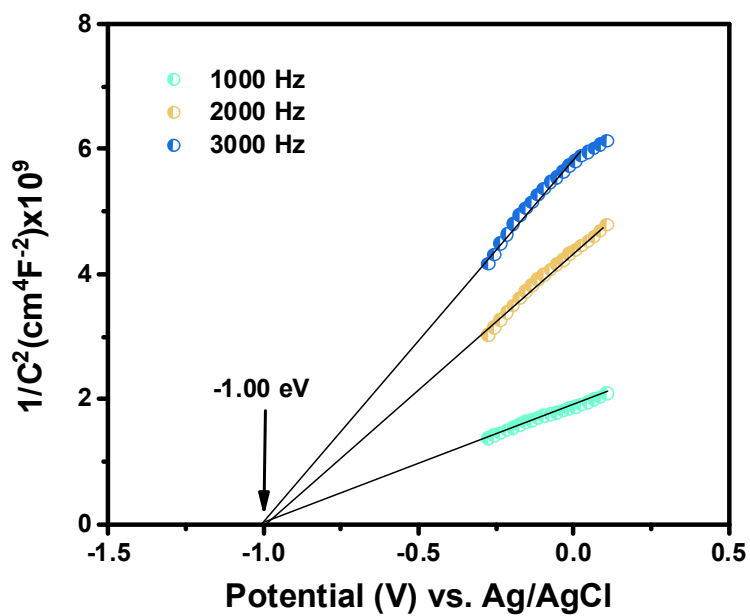

Fig. S18 Mott-Schottky plot of **HL**.
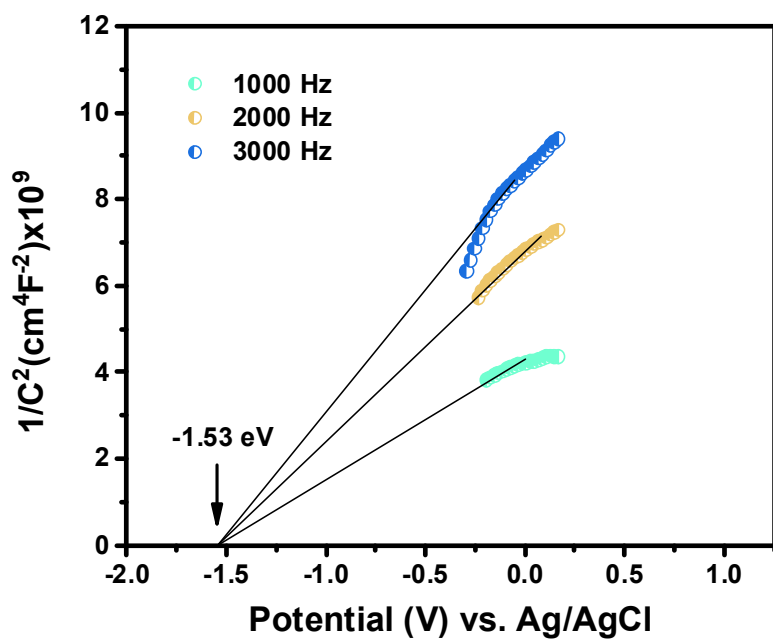

Fig. S19 Mott-Schottky plot of **1.**
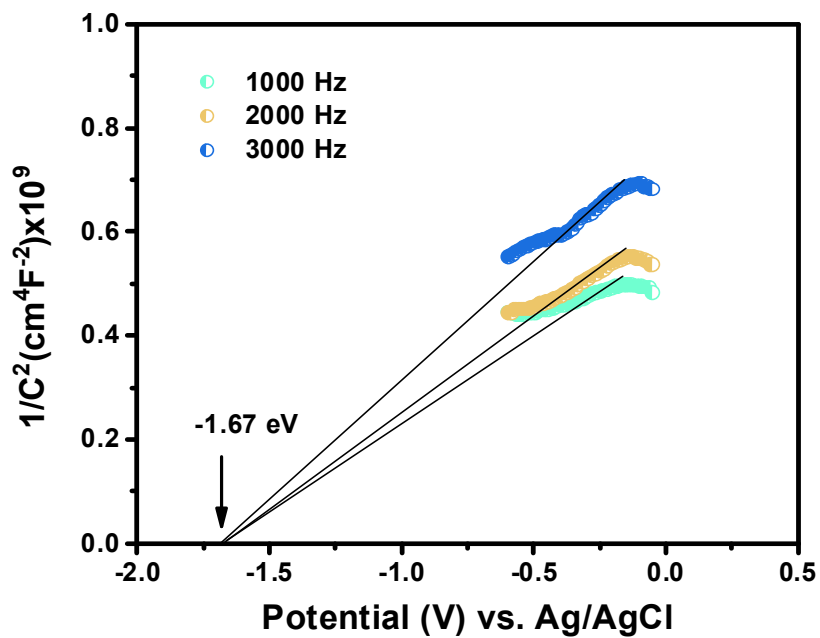
Fig. S20 Mott-Schottky plot of **2.**

Fig. S21 Mott-Schottky plot of **3.**
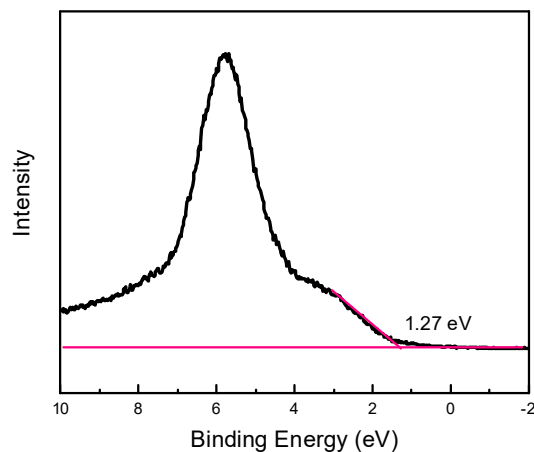
2.11 Valence band spectrum measurement

Fig. S22 Valence band spectrum of **1**. The corresponding E_{VB} XPS of **1** is measured to be 1.27 eV. Then, the E_{VB} vs. standard hydrogen electrode (E_{VB}, NHE) can be calculated according to the following formula[6]: E_{VB} NHE = φ + E_{VB} XPS – 4.44. where φ is the work function of the instrument (4.2 eV). Thus, the E_{VB} NHE of **1** is calculated to be 1.03 eV.

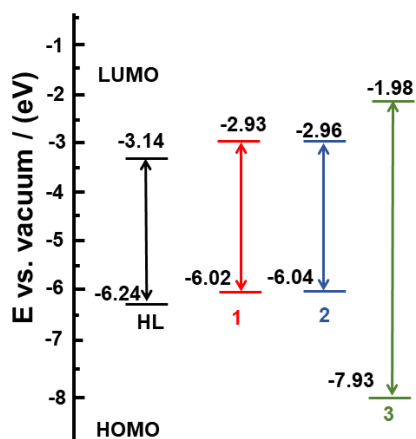**2.12 Energy gap from theoretical calculation**

Fig. S23 The calculated energy level diagram (LUMO and HOMO) of structures of photocatalysts including **HL**, **1**, **2** and **3** (eV vs. vacuum), where LUMO and HOMO represent the lowest unoccupied molecular orbital and highest occupied molecular orbital.
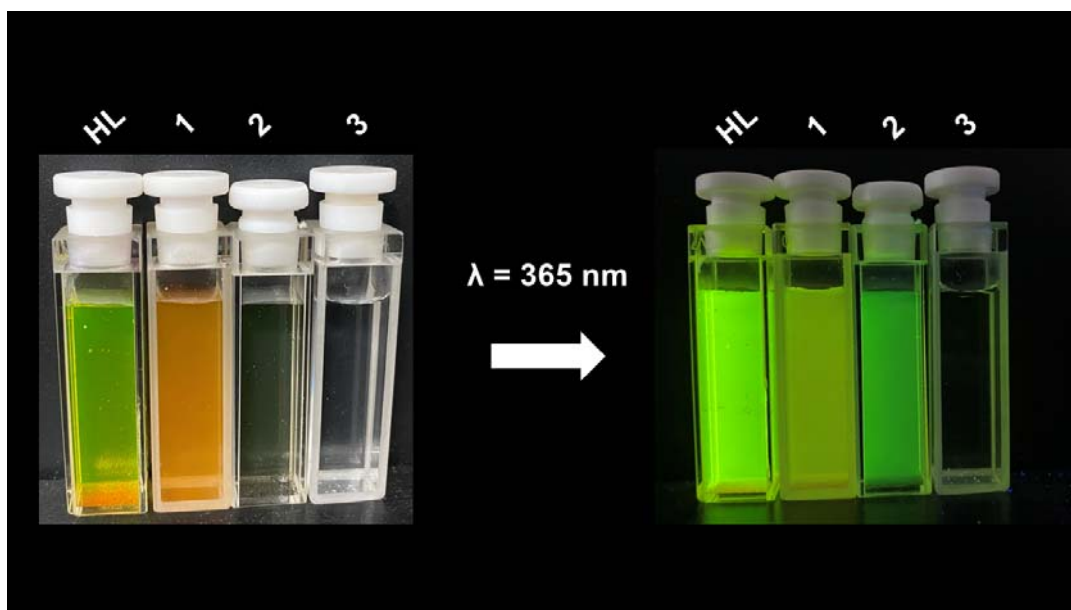
2.13 Photoluminescence (PL) properties

Fig. S24 The images of **HL**, **1**, **2**, and **3** in water-suspended solutions under sunlight (left) and a hand-held UV lamp (right).
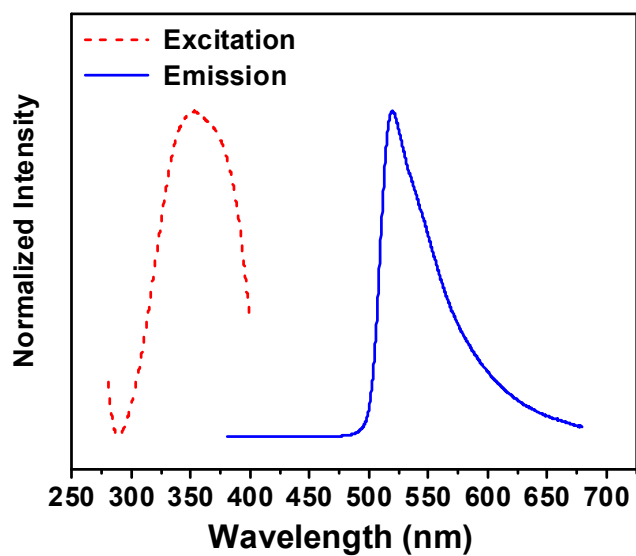

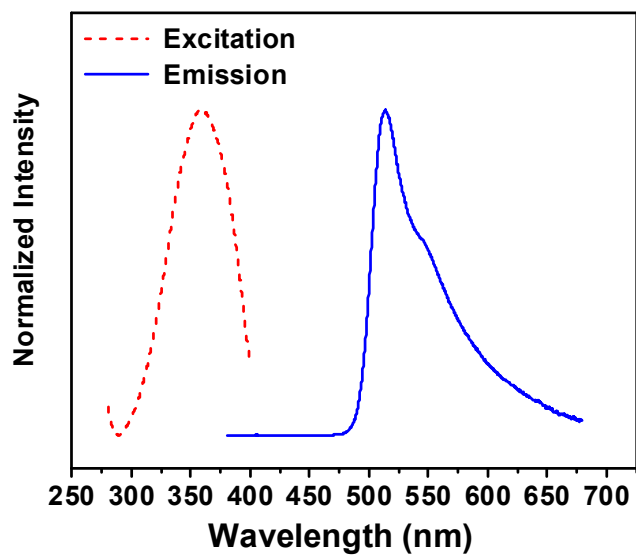**Fig. S25** The normalized emission and excitation spectra of **HL**.

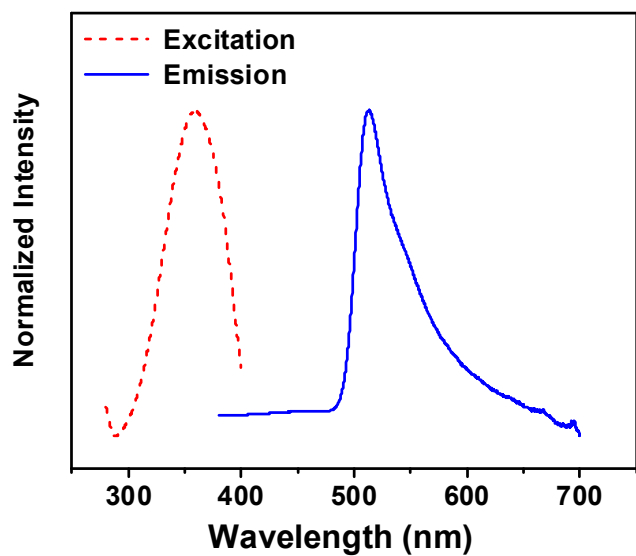**Fig. S26** The normalized emission and excitation spectra of **1**.

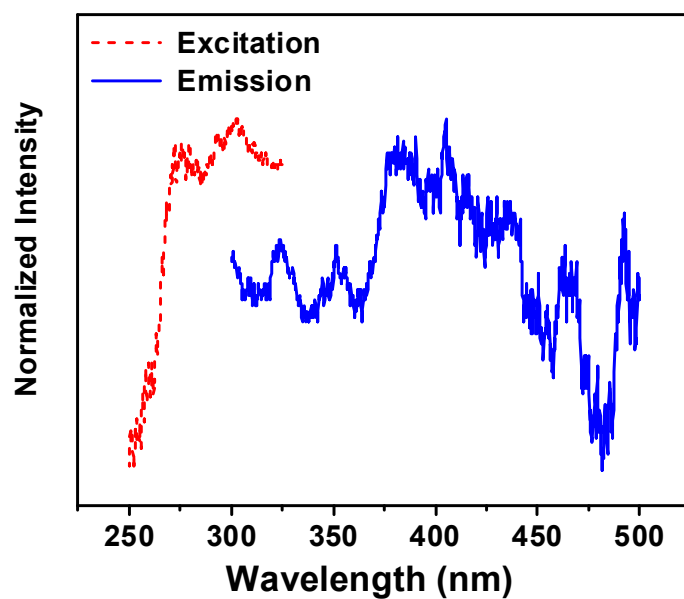**Fig. S27** The normalized emission and excitation spectra of **2**.

Fig. S28 The normalized emission and excitation spectra of **3**.

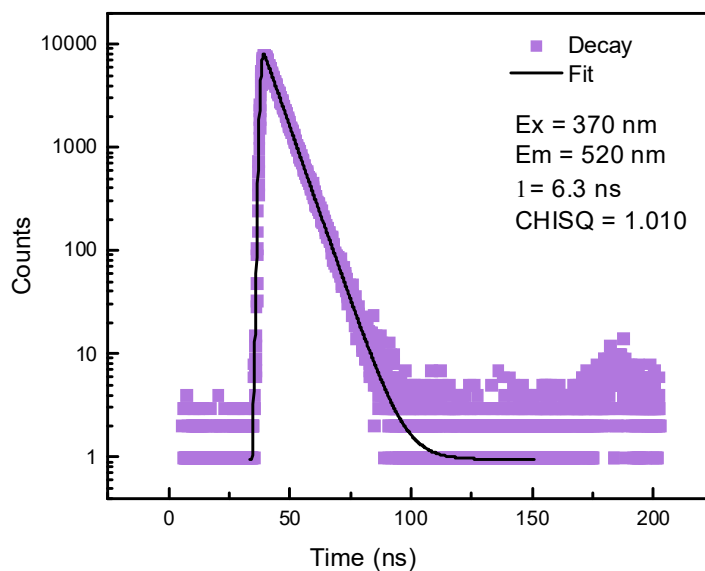## 2.14 Room-temperature photoluminescence lifetime

Fig. S29 Photoluminescence decay of **HL** at film-state obtained via time-correlated single photon counting (purple), and the black line represents a dual-exponential fit of the data.

Fig. S30 Photoluminescence decay of **1** at film-state obtained via time-correlated single photon counting (red), and the black line represents a dual-exponential fit of the data.

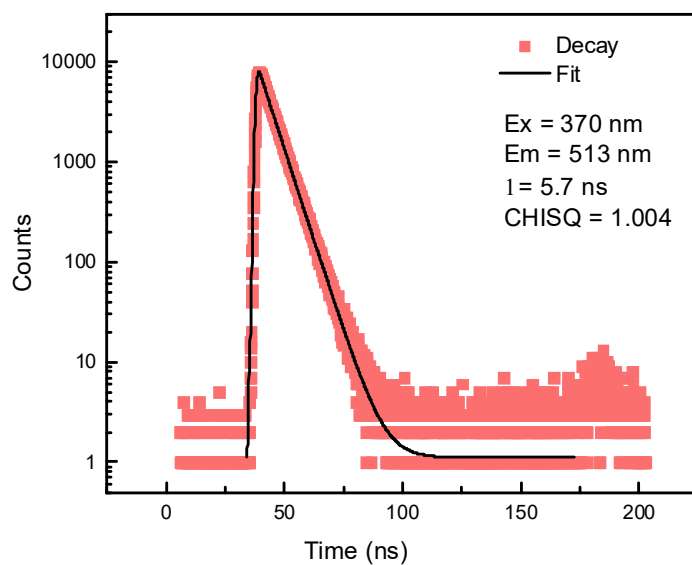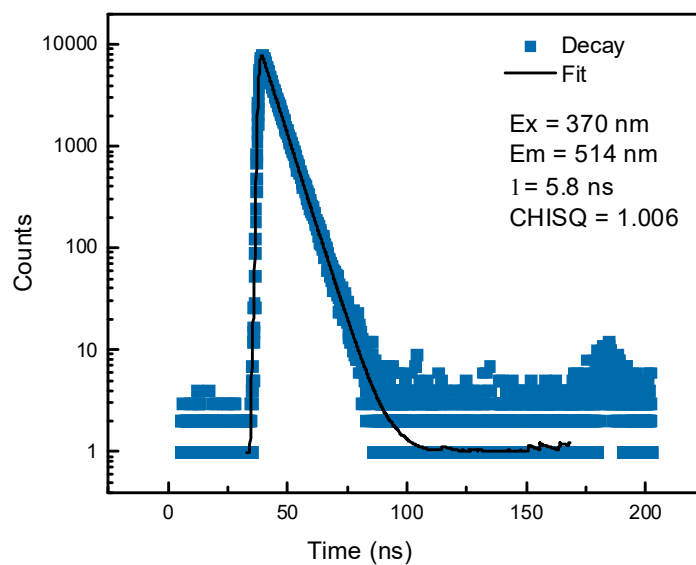**Fig. S31** Photoluminescence decay of **2** at film-state obtained via time-correlated single photon counting (blue), and the black line represents a dual-exponential fit of the data.
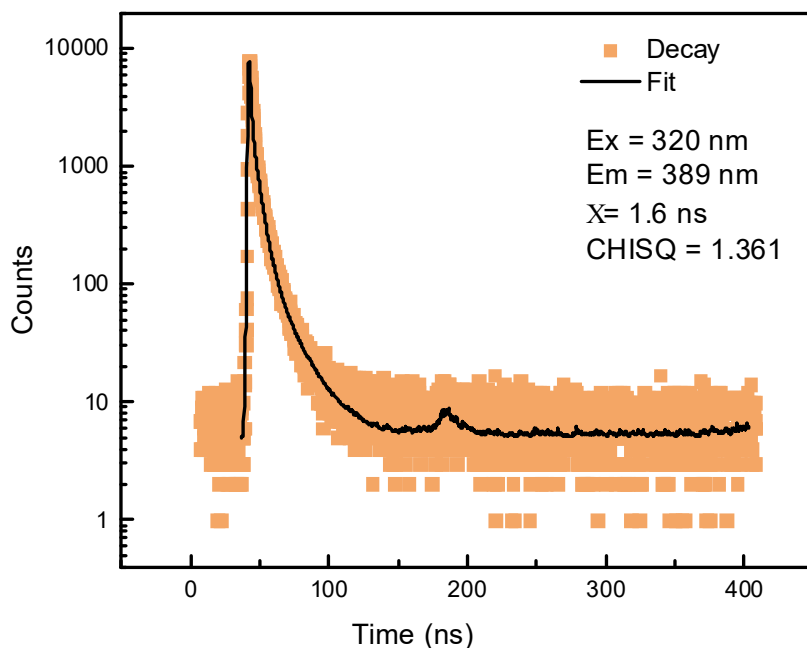
Fig. S32 Photoluminescence decay of **3** at film-state obtained via time-correlated single photon counting (yellow), and the black line represents a triple-exponential fit of the data.

Table S2 Summary of photophysical parameters for the compounds in the suspended state

Complexes	λ_{ex}	λ_{em}	Φ_F (%)[a]	τ_T (ns)[f]
HL	352	520	80.2[b]	6.3[g]
1	356	514	36.5[c]	5.7[g]
2	358	514	79.2[d]	5.8[g]
3	275	389	0.4[e]	1.6[h]

[a] Fluorescence quantum yields. [b] λ_{ex} = 320 nm. [c] λ_{ex} = 350 nm. [d] λ_{ex} = 340 nm. [e] λ_{ex} = 260 nm. [f] The average fluorescence decay lifetime. [g] λ_{ex} = 370 nm. [h] λ_{ex} = 320 nm.
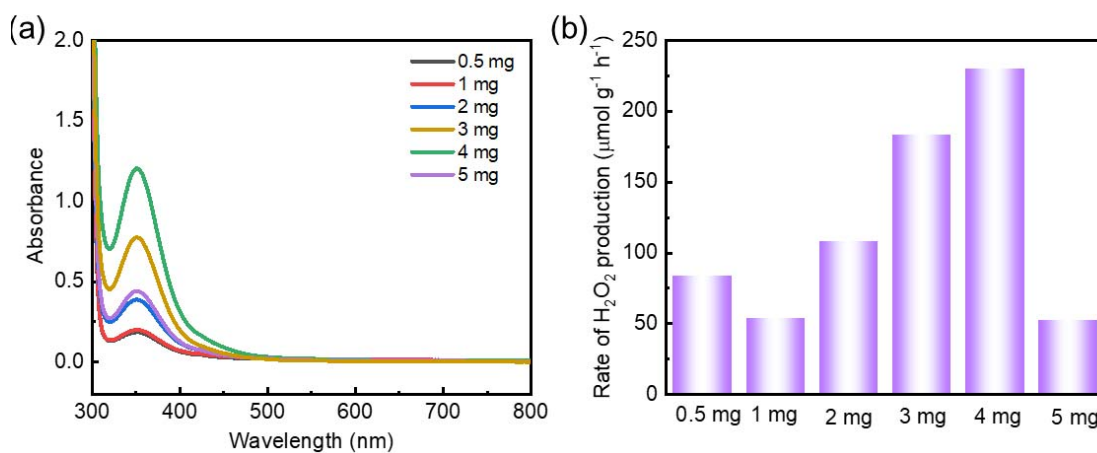
2.15 Photo-catalytical experiment

Fig. S33 (a) UV-vis absorption spectra of I_3^- from reaction solution treated by iodometry with different amounts of photocatalyst **1**. (b) Comparison chart of H_2O_2 production rate with different amounts of photocatalyst **1**. (To reach the reaction equilibrium, the reaction solution was stood at rt for 12 hours. Afterward the UV-vis absorption spectra were recorded.)
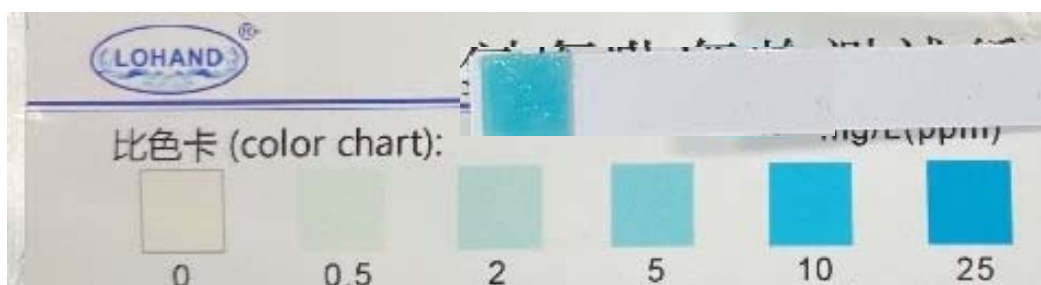

Fig. S34 The measurement of photocatalytic H_2O_2 production activities by H_2O_2 test strips (picture is measurement after photocatalysis). Test conditions: photocatalysts **1**: 4 mg in 5 mL water; air condition: O_2; light source =300 W Xenon lamp; irradiation time = 5 hours, the scale bar is mg/L (ppm).
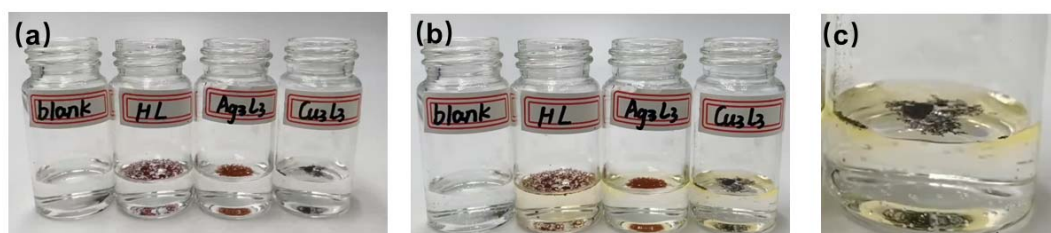
Fig. S35 The pictures of **HL**, **1** (Ag₃L₃), and **2** (Cu₃L₃) in 3wt% H₂O₂ suspension at (a) 0 min, and (b) 0.5 h, suggesting the Cu-CTC **2** can catalyze the decomposition of H₂O₂. (c) The enlarged image of **2** (Cu₃L₃) in (b) showing the bubble and the color of solution turn to yellow.

Continuous Ar atmosphere: To rule out the possibility of $2e^-$ WOR, the photocatalytic reactions have been conducted under continuous argon gas inflow conditions. Specifically, to 5 mL of H₂O, complex **1** (4 mg) was added, and the resulting mixture was photoirradiated for 5 h at rt. The continuous argon gas flow can remove the O₂ generated from the $4e^-$ OER, which can prohibit the ORR to produce H₂O₂ under Ar atmosphere. If the $2e^-$ WOR occurred, the H₂O₂ should be detected under continuous argon gas inflow conditions. However, no H₂O₂ has been detected after 5h photoirradiation, suggesting the $2e^-$ WOR did not occur.
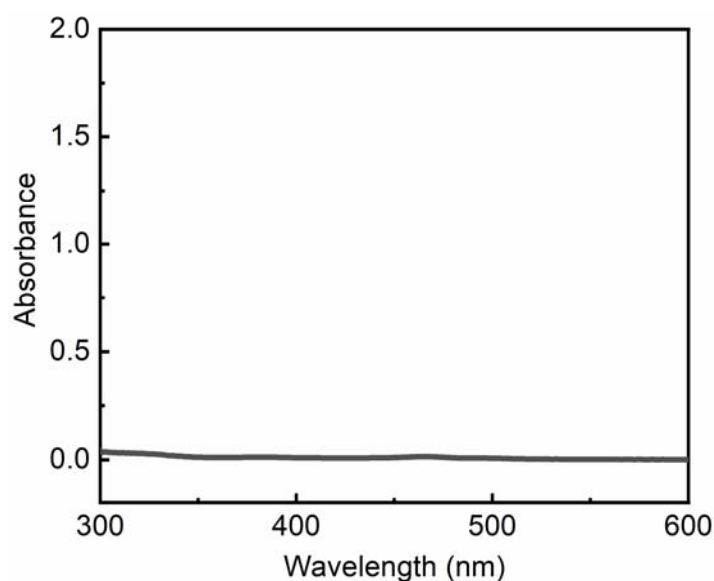

Fig. S36 (a) UV-vis absorption spectra of I_3^- from catalytic reaction solution treated by iodometry photocatalyst **1** under continuous Ar atmosphere for 5 h (To reach the reaction equilibrium, the reaction solution was stood at rt for 12 hours. Afterward the UV-vis absorption spectra were recorded.)

Fig. S37 (a) UV-vis absorption spectra of I_3^- from catalytic reaction solution treated by iodometry photocatalyst **1** with different scavengers. (b) Comparison chart of H_2O_2 production rate with different scavengers. (To reach the reaction equilibrium, the reaction solution was stood at rt for 12 hours. Afterward the UV-vis absorption spectra were recorded.)

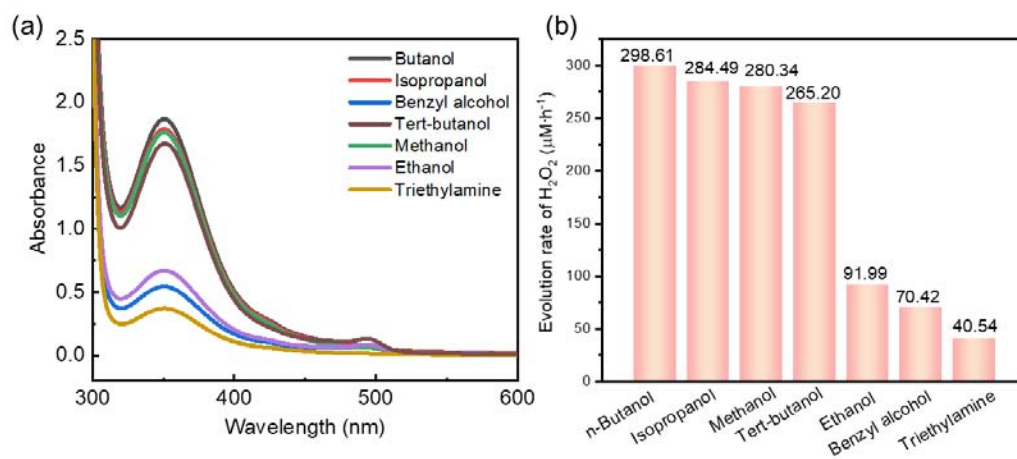**Fig. S38** Wavelength-dependent AQY values (measured in the first 1 h) and solid-state UV-visible spectrum of **1**.

Fig. S39 (a) UV-vis absorption spectra of I_3^- from catalytic reaction solution treated by iodometry photocatalyst **1** with different light radiation time (To reach the reaction equilibrium, the reaction solution was stood at rt for 12 h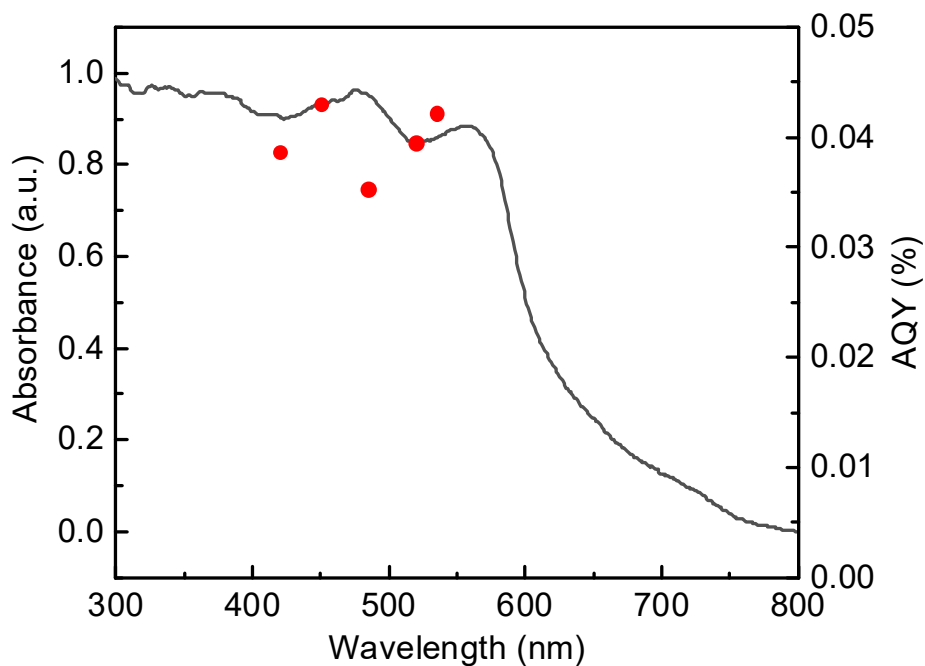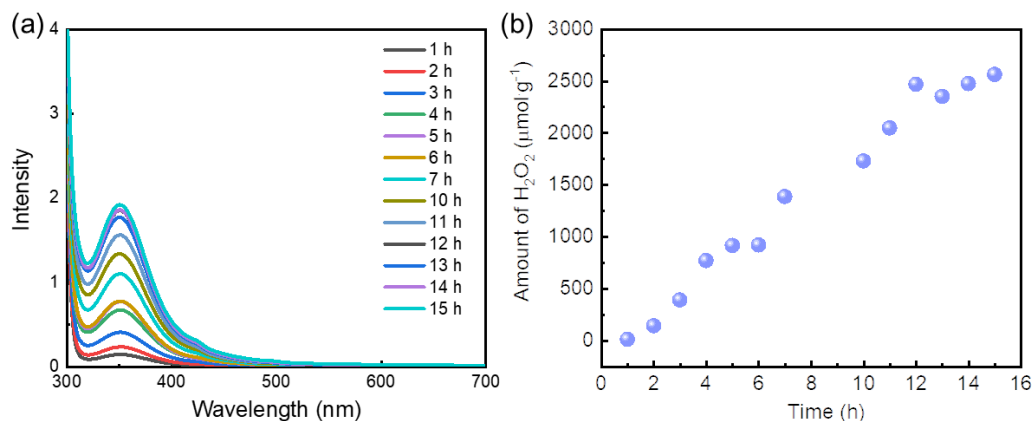ours. Afterward the UV-vis absorption spectra were recorded). (b) Long-term H_2O_2 production profile. Test conditions: photocatalysts **1**: 9 mg in 15 mL water; air condition: O_2; light source =300 W Xenon lamp.
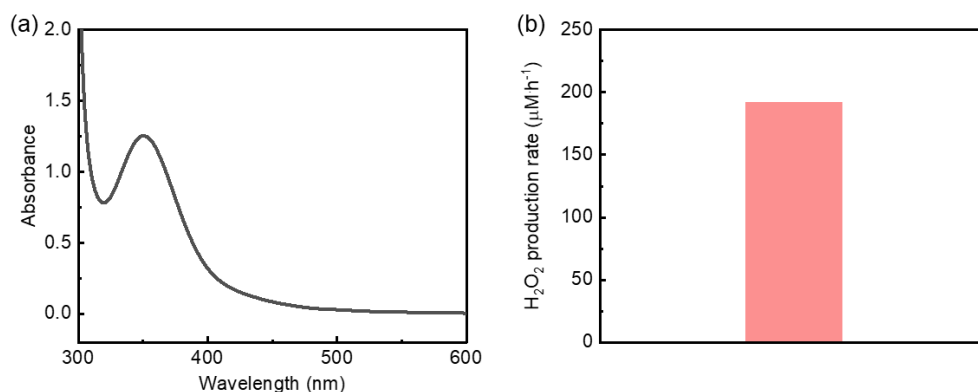

Fig. S40 (a) UV-vis absorption spectrum of I_3^- from catalytic reaction solution treated by iodometry photocatalyst **1** using seawater (To reach the reaction equilibrium, the reaction solution was stood at rt for 12 hours. Afterward the UV-vis absorption spectra were recorded). (b) The H_2O_2 production rate. Test conditions: photocatalysts **1**: 4 mg in 5 mL seawater; air condition: O_2; light source =300 W Xenon lamp. The final result is the average of three experimental trials.
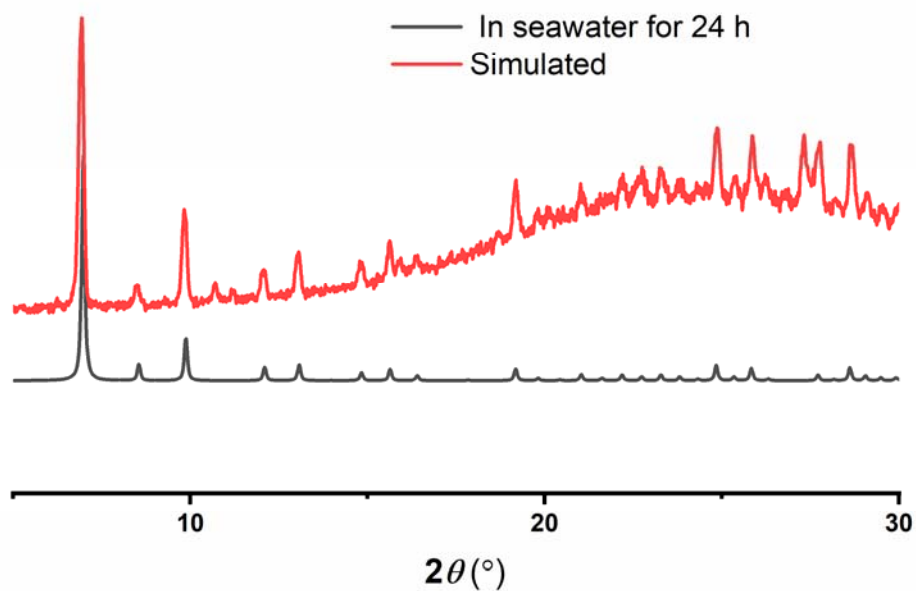
Fig. S41 Comparison of PXRD patterns of the photocatalyst **1** before and after treatment of seawater for 24 h.
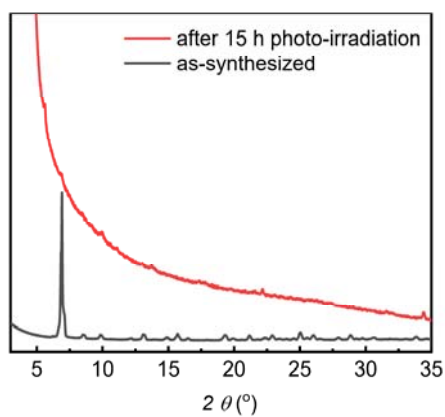

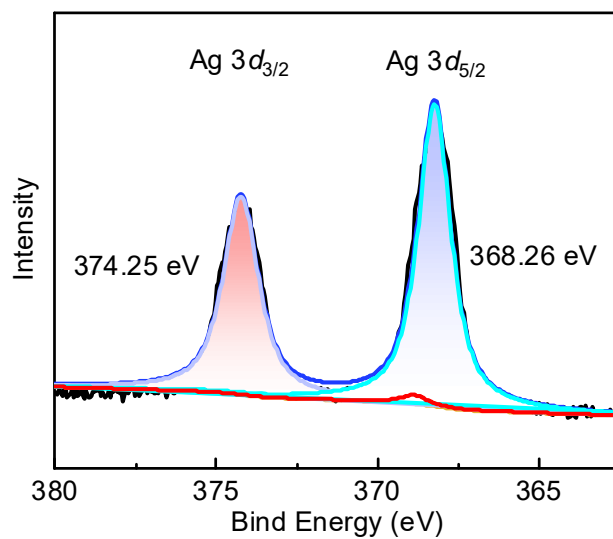**Fig. S42** PXRD patterns of 1 before and after 15 h photo-irradiation

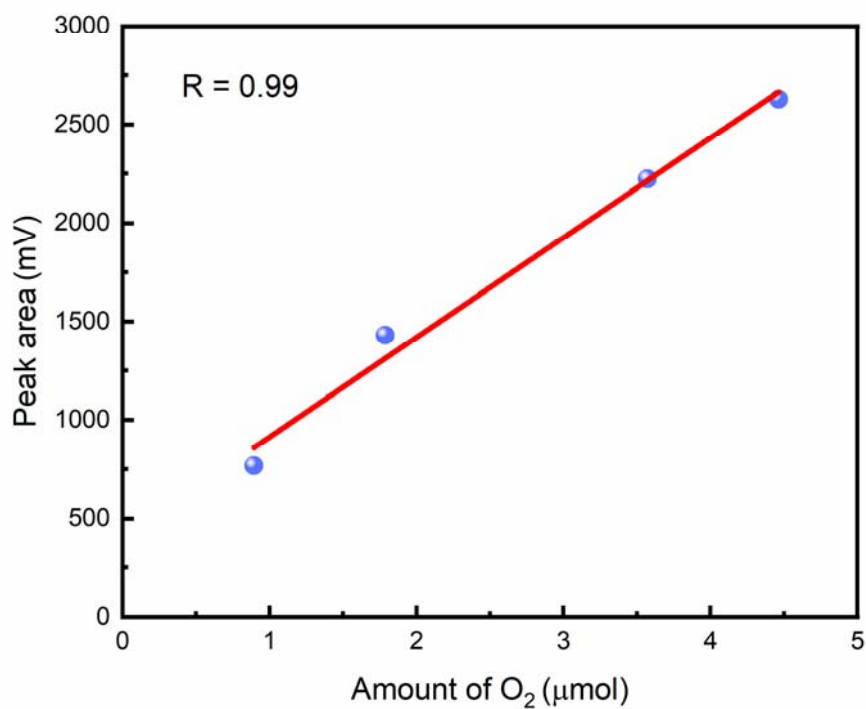**Fig. S43** XPS for **1** after photocatalysis, suggesting the valence of Ag remain intact.
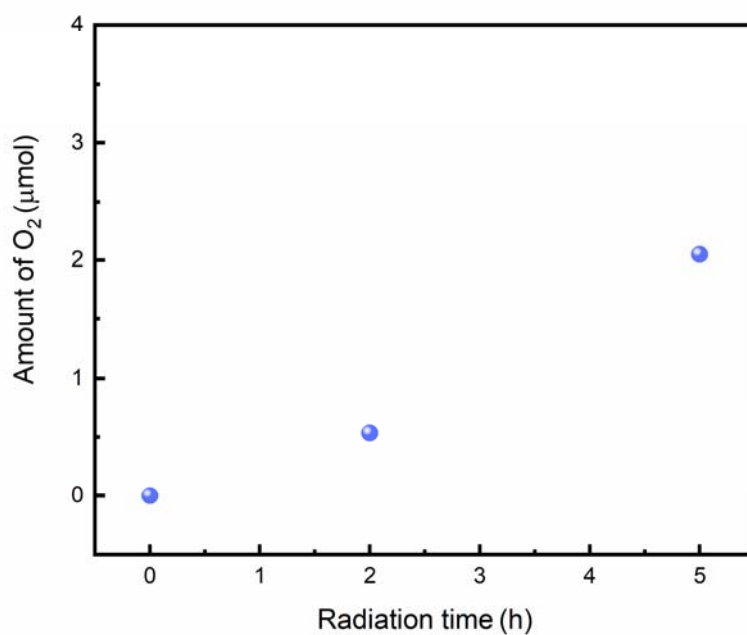

Fig. S44 The criterion curve of O₂.

Fig. S45 O_2 production in the half-reaction of photocatalyst **1**. Reaction conditions: 5 mg photocatalyst **1**, 10 mL pure water, 20 mM $NaIO_3$ and 20 mg La_2O_3 in Ar under visible light illumination (300 W Xe lamp with a $\lambda > 420$ nm filter).

Table S3 Optimate experiment of oxygen evolution reaction

Entry	Photocatalyst (mg)	La_2O_3 (mg)	$AgNO_3$ (mg)	$NaIO_3$ (mg)	H_2O (mL)	Reaction time (h)	Oxygen evolution rate (μmol /g /h)
1	5	20	20	–	10	5	42.8
2	5	–	–	20	10	5	0.4
3	5	10	–	20	10	5	9.6
4	5	20	–	20	10	5	81.8

2.17 Isotopic exchange experiments

H$_2^{18}$O isotopic experiment: 1 mg of photocatalyst 1, 0.5 mL of H$_2^{18}$O, 1 mg NaIO$_3$ (electron scavenger), and 1 mg La$_2$O$_3$ were added into a 10 mL vial, which was then sealed with a rubber septum and purged with Ar gas for 1 h. The vial was then irradiated with a xenon lamp equipped with a filter (λ>420 nm) for 12 hours, and the gas produced was detected using the Agilent 7890B GC-MS system. For the control experiment, the same procedure was followed except for the absence of irradiation and compound **1**. Indeed, the ^{18}O$_2$ can be detected, and thus indicate the complex **1** can photo-oxidize water to produce O$_2$.

H$_2^{18}$O and ^{16}O$_2$ isotopic experiment: 5 mg of photocatalyst **1** and 0.5 mL of H$_2^{18}$O were added into a 10 mL vial, which was then sealed with a rubber septum and purged with ^{16}O$_2$ gas for 15 min. The vial was then irradiated with a xenon lamp equipped with a filter (λ>420 nm) for 12 hours, followed by another purge with argon gas to remove the ^{18}O$_2$ gas. The reaction solution was then transferred to another 10 mL vial containing MnO$_2$ and argon gas for 1 hour to remove ^{16}O$_2$, and the gas produced during the decomposition of hydrogen peroxide was analyzed using the Agilent 7890B GC-MS system. For the control experiment, the same procedure was followed except for the absence of irradiation and compound **1**.
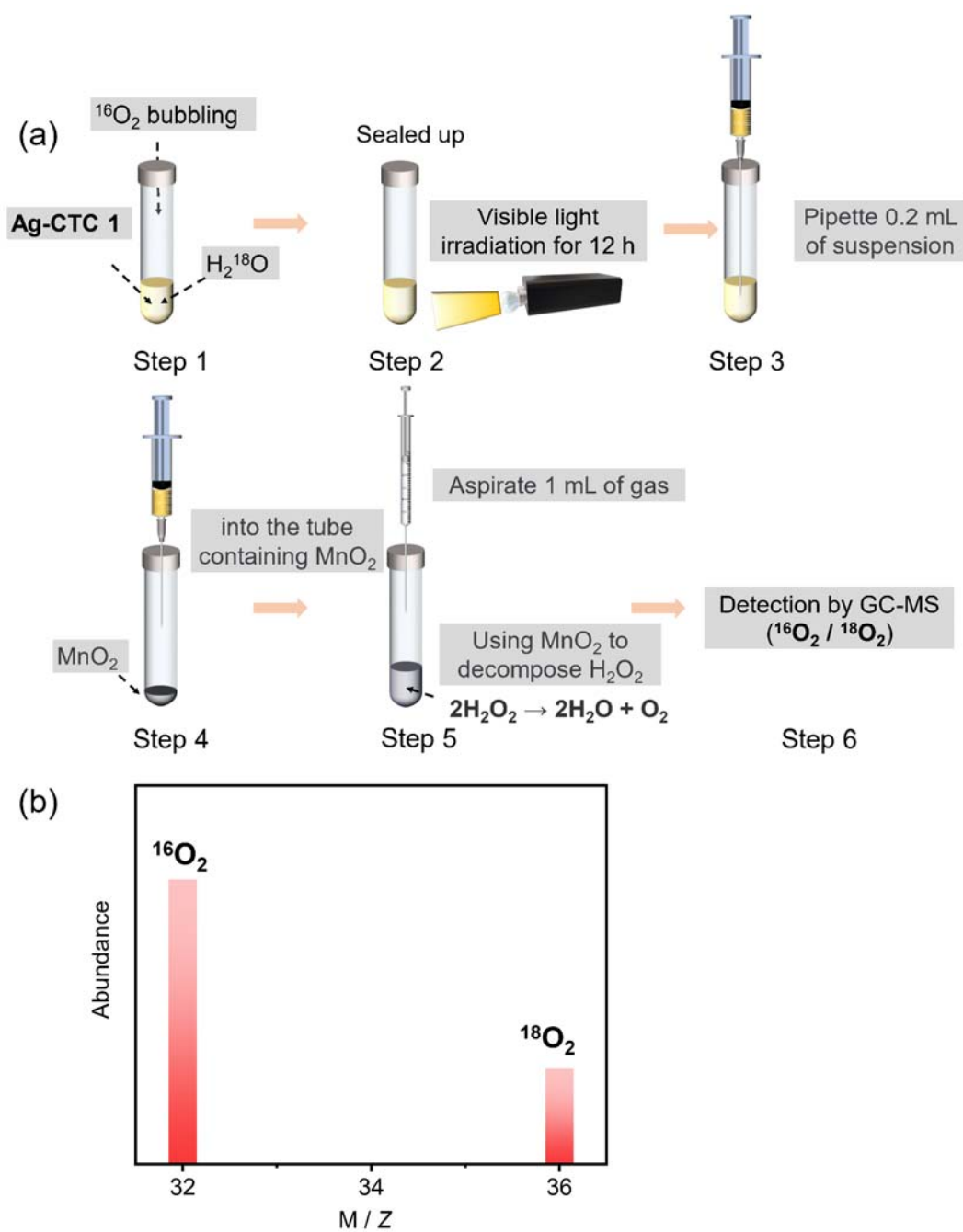
Fig. S46 (a) Schematic diagram showing the isotope experimental procedure for H_2O_2 production in pure water ($H_2^{18}O$)**,** (b) GC-MS spectra of the gas decomposition of photogenerated hydrogen peroxide by photocatalyst **1**, showing the content of $^{18}O_2$ can be detected from $H_2^{18}O_2$.

$^{18}O_2$ isotopic experiment: 5 mg of photocatalyst **1** and 1.5 mL of $H_2^{16}O$ were added into a 10 mL vial, which was then sealed with a rubber septum and purged with argon gas for 1 hour to remove $^{16}O_2$. Subsequently, 10 mL of $^{18}O_2$ gas (purity: 99%) was injected into the vial using a syringe. The vial was then irradiated with a xenon lamp equipped with a filter (λ>420 nm) for 5 hours and 10 hours, followed by another purge with argon gas to remove the $^{18}O_2$ gas. The reaction solution was then transferred to another 10 mL vial containing MnO_2 and argon gas, and the gas produced during the decomposition of hydrogen peroxide was analyzed using the Agilent 7890B GC-MS system. For the 0-hour experiment, the same procedure was followed except for the absence of irradiation and compound **1**.

NOTE: Since the gas sample was injected into the GC through a syringe, the $^{16}O_2$ come from the air.
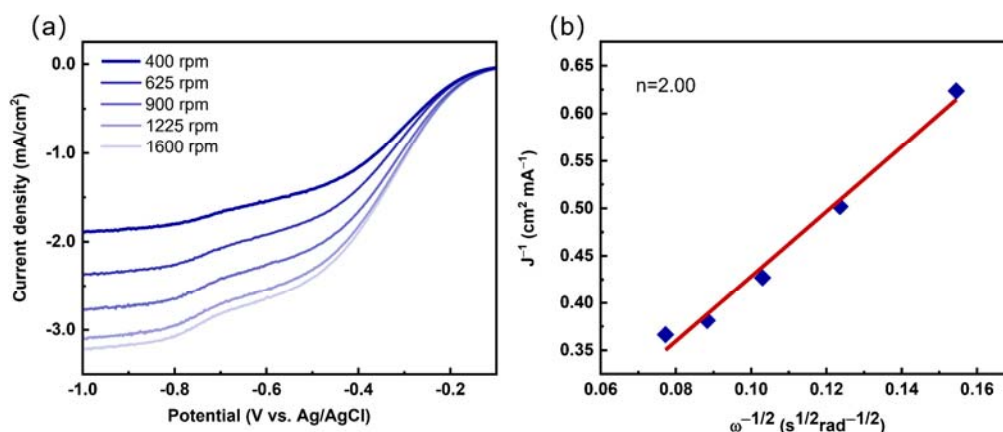
2.18 RDE measurement

Fig. S47 (a) Different rotating speeds of linear-sweep RDE voltammograms of the photocatalyst **1** and (b) The Koutecky–Levich plots obtained by RDE measurements at −0.65 V (vs. Ag/AgCl).
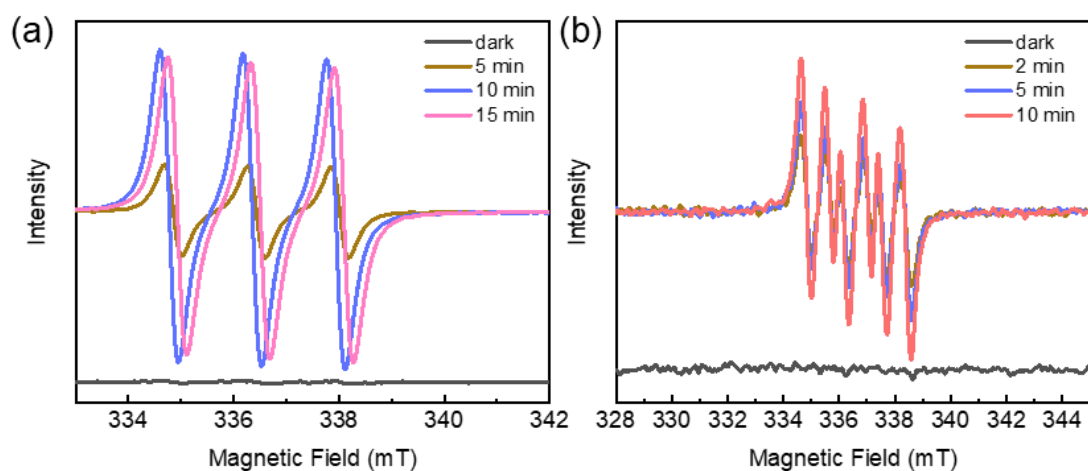
2.19 EPR experiment

Fig. S48 EPR signals of (a) $^1O_2$ and (b) $O_2^{\bullet-}$ using HL as photocatalyst under dark and visible light radiation with different time.
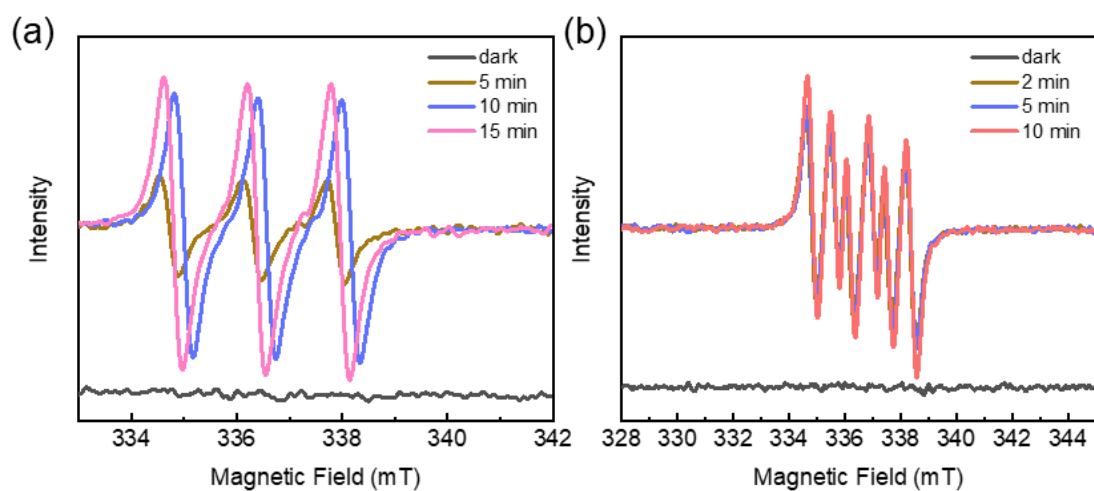

Fig. S49 EPR signals of (a) $^1O_2$ and (b) $O_2^{\bullet-}$ using **1** as photocatalyst under dark and visible light radiation with different time.
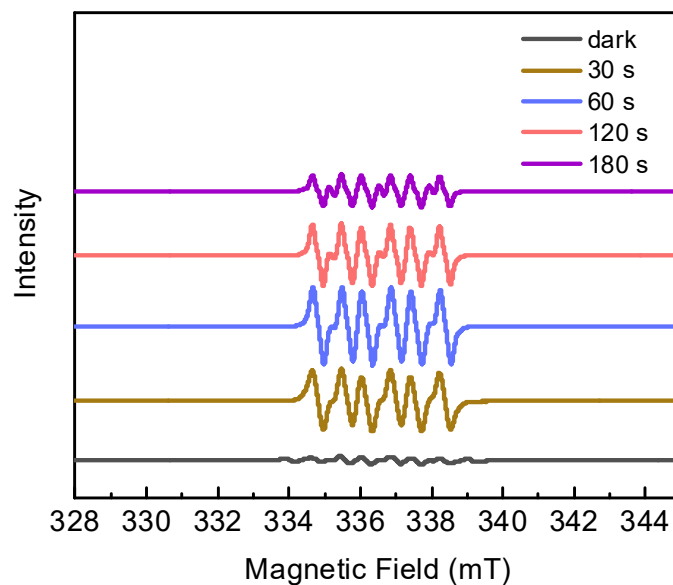
Fig. S50 EPR signals of $O_2^{\bullet-}$ using **2** as photocatalyst under dark and visible light radiation with different time.
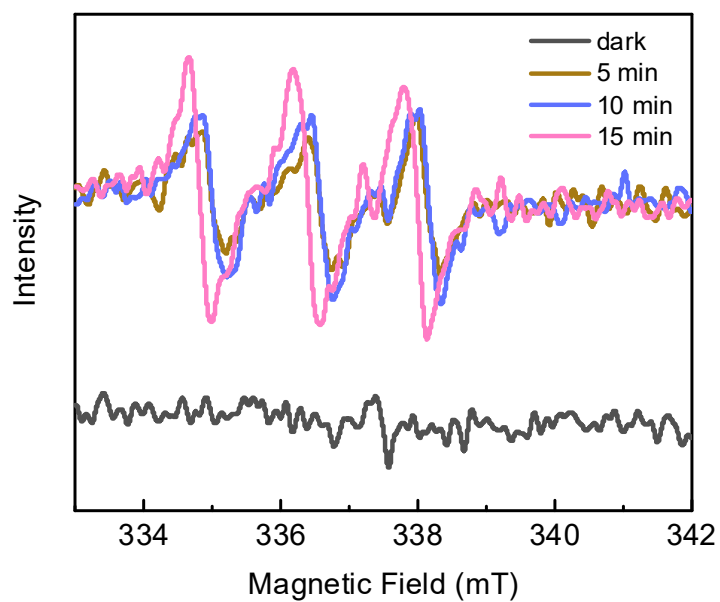

Fig. S51 EPR signals of O_2 using **3** as photocatalyst under dark and visible light radiation with different time.
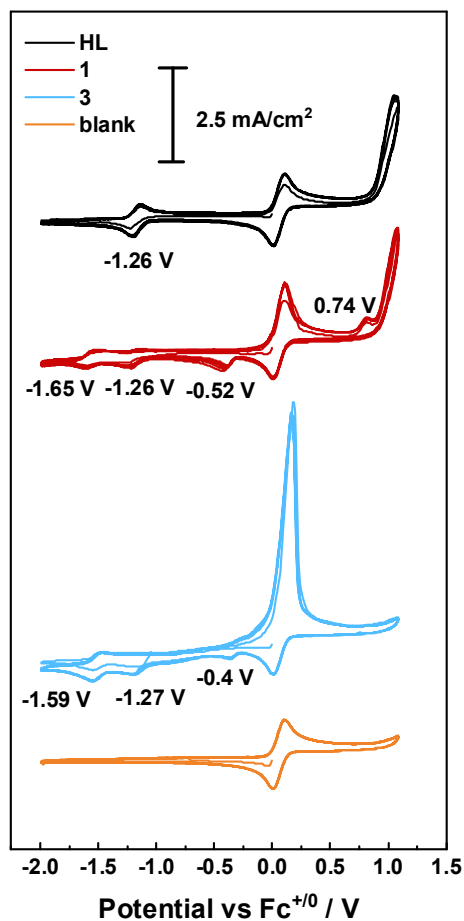
2.20 Cyclic Voltammetry (CV) test

Fig. S52 CV curves of **HL**, **1**, **3** and blank Ferrocene (Fc). The experiments were carried out in deaerated DMF solution, containing 0.5 mM of **HL**, **1**, or **3**, 0.2 mM Fc, and 0.10 M Bu_4NPF_6 as the supporting electrolyte, with a scan rate of 0.05 V/s^{-1} and a negative initial scan direction. Glassy carbon electrode, $Ag/AgNO_3$, and Pt silk were used as the working electrode, reference electrode, and counter electrode, respectively.

Section S3. Computational Details

3.1 DFT

Density functional theory (DFT), Time-dependent density-functional theory (TDDFT) and free energy were performed for **HL**, **1**, **2** and **3** by using Gaussian 09 software.[7] The following level of theory was adopted in all the calculations: (1) Functional: the hybrid Perdew, Burke, and B3LYP in conjunction with D3(BJ) dispersion correlation;[8, 9] (2) Basis sets: the LANL2DZ[10-13] effective core potential (ECP) was used for Cu, Ag and the 6-31G(d,p)[14] basis set was used for the other atoms. The geometrical optimization was performed for the monomers of all the above compounds to obtain their stable ground-state (S$_0$) geometries by the B3LYP method, confirmed by the absence of imaginary frequencies. After geometrical optimization, the following computations were carried out. Electrostatic potential (ESP) surfaces were drawn for the monomer of complex **1**, by mapping ESP on the van der Walls isosurfaces of the model with isovalue = 0.03 a.u. TDDFT calculations were performed for the first 50 singlet-singlet spin-allowed transitions and the first 10 singlet-triplet spin-forbidden transitions were calculated based on the optimized S$_0$ structures. By using Multiwfn program,[15] the TDDFT results were extracted from the Gaussian output files (log files), and the cub files for drawing the electron density differences (EDD) maps were obtained by the hole-electron analysis function[16] of Multiwfn software after inputting the log files and the formatted checkpoint (fchk) files. The isovalue of EDD maps was 0.0004 a.u.

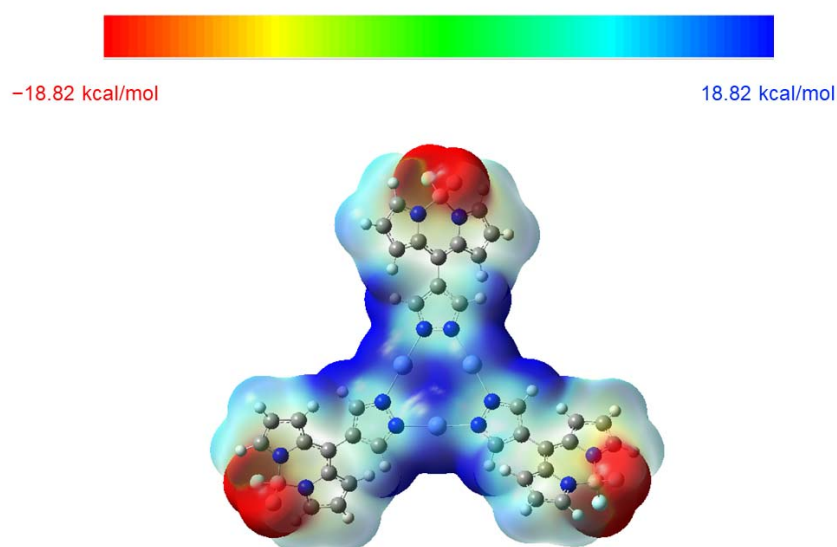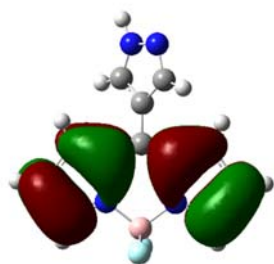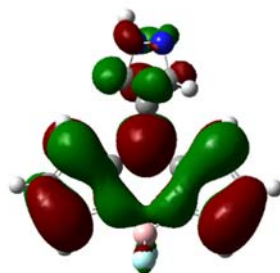−18.82 kcal/mol   18.82 kcal/mol

Fig. S53 The Electrostatic Potential Surfaces (ESP) of **1** indicates the distribution of its electrons with the scale range from red to blue (units in kcal mol^{-1}).
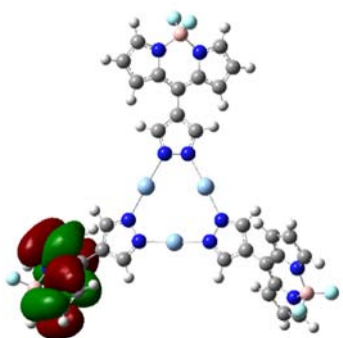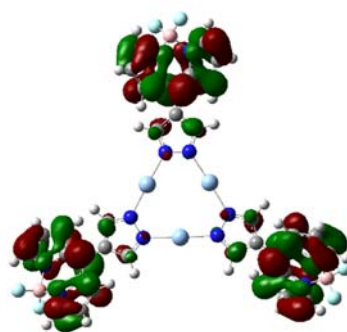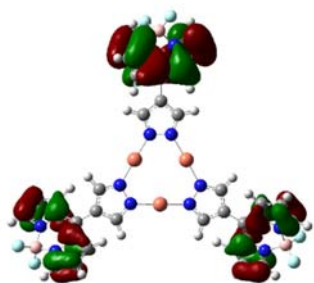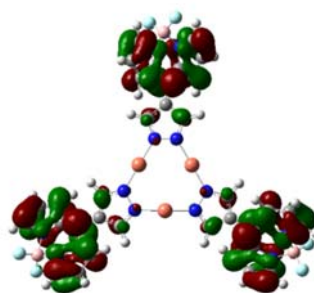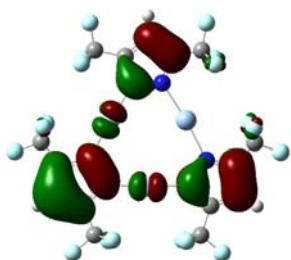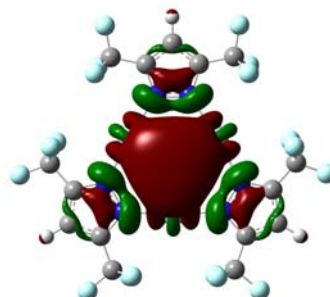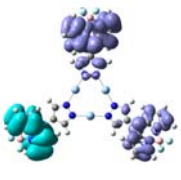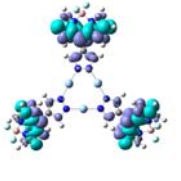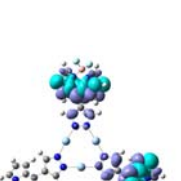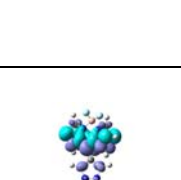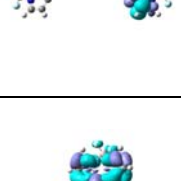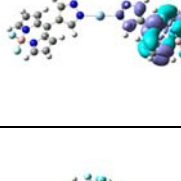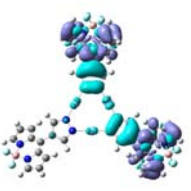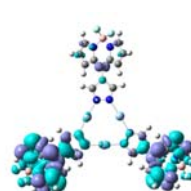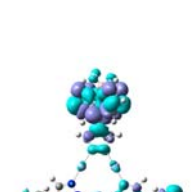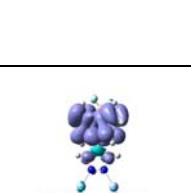
Fig. S54 (a) HOMO and (b) LUMO of **HL**; (c) HOMO and (d) LUMO of **1**; (e) HOMO and (f) LUMO of **2**; (g) HOMO and (h) LUMO of **3**, which estimated from DFT calculations using the B3LYP/6-31G (d,p) basis set.

Table S4 The selected singlet-singlet spin-allowed transitions of complex **1** at B3LYP-D3(BJ) / (LANL2DZ + 6-31G(d,p)) level[a]

No.	E(eV)	λ(nm)[b]	f[c]	EDD maps[d]	Main transitions
1	2.8635	432.98	0.00020		H → L 84.5% H → L+2 14.3%
7	3.0777	402.85	0.0570		H → L+2 31.0% H-2→L 15.6% H-1→L+1 12.9% H-2→ L+1 9.6% H → L 6.1%
8	3.0832	402.13	0.19500		H-1→ L+1 31.7% H → L+2 29.4% H-1 → L 10.7% H-1 → L+2 6.7% H-5 → L+2 5.9% H-6 → L+1 5.4%
9	3.0938	400.75	0.60770		H-2 → L 31.9% H-2 → L+1 22.0% H-1 → L+1 9.3% H → L+2 8.7% H-7 → L 6.8%
11	3.5401	350.23	0.08190		H-5 → L+2 33.1% H-6 → L+1 27.2% H-6 → L 13.1% H → L+2 6.2% H-1 → L+1 5.6%
12	3.5465	349.60	0.33850		H-7 → L 30.2% H-7 → L+1 15.8% H-6 → L+1 9.0% H-5 → L+2 8.6% H-2 → L 5.8%

13	3.5853	345.81	0.30810		H-4 → L 43.4% H-8 → L+1 14.3% H-3 → L+2 10.8% H-3 → L+1 5.3%
14	3.5866	345.69	0.32160		H-3 → L 23.6% H-3 → L+1 19.2% H-8 → L+2 13.9% H-3 → L+2 11.3% H-4 → L+2 8.9% H-4 → L+1 6.7%
19	3.7146	333.78	0.30810		H-10 → L 27.3% H-11 → L+1 27.1% H-11 → L 13.9% H-4 → L 8.5% H-9 → L+2 5.6%
20	3.7150	333.74	0.29810		H-9 → L+2 19.5%\ H-9 → L 17.8% H-10→ L+2 15.2% H-10→ L+1 10.4% H-9 → L+1 10.1% H-11 → L+2 9.0% H-3 → L 5.4%
33	3.9654	312.67	0.02400		H-8 → L+2 77.8% H-3 → L+2 5.3%

[a] Only the TDDFT results of the S_1 state and the S_n states with f larger than 0.01 among the first 10 S_n states were given. [b] The wavelengths. [c] Oscillator strength. [d] Isovalue = 4×10^{-4} a.u. The electrons transfer from the blue regions to the purple regions during the excitation from the S_0 state to the S_n state.

3.2 Adsorption Energy (ΔE_{ad})

For the H_2O_2 production process, O_2 and H_2O molecules are absorbed on the surface of photocatalysts, and adsorption free energy ΔE_{ad} was used to estimate the strength of adsorption. The ΔE_{ad} is defined as:

$$\Delta E_{ad} = E_{mol/sub} - E_{mol} - E_{sub} \qquad\qquad (1)$$

Where $E_{mol/sub}$ is the total energy of the adsorbed system, E_{mol} is the energy of an isolated molecule, and E_{sub} is the energy of a clean metal substrate.[17]
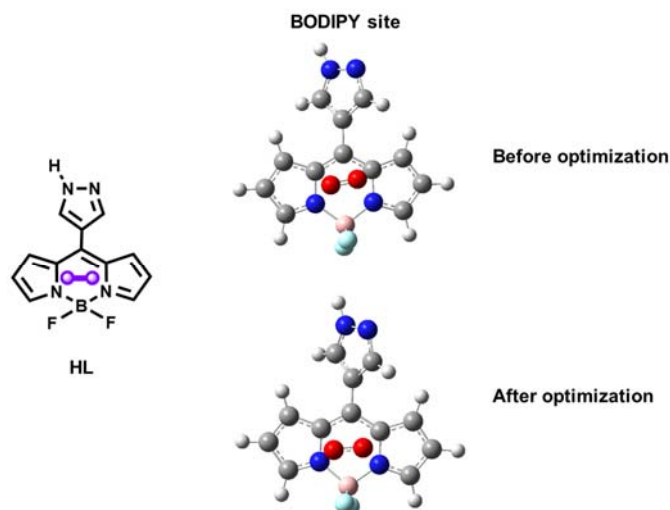
Fig. S55 The adsorption of O_2 on BODIPY site of **HL**.
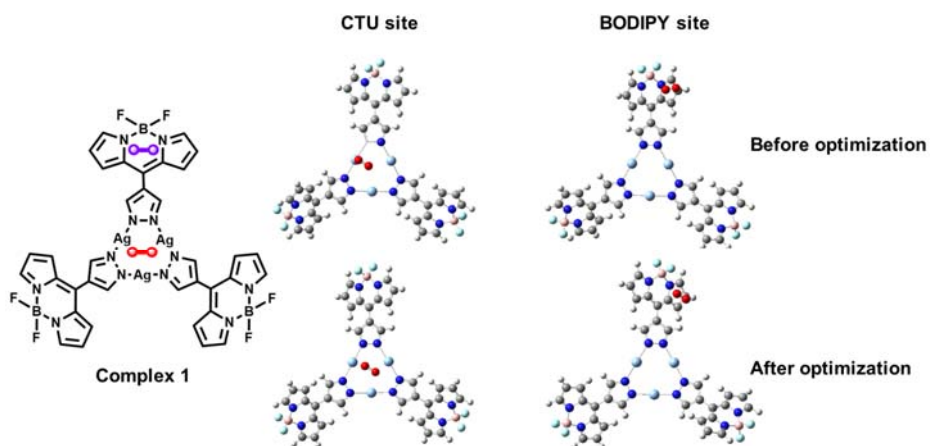
Fig. S56 The adsorption of O_2 on the BODIPY site and Ag_3N_6 site of **1**.
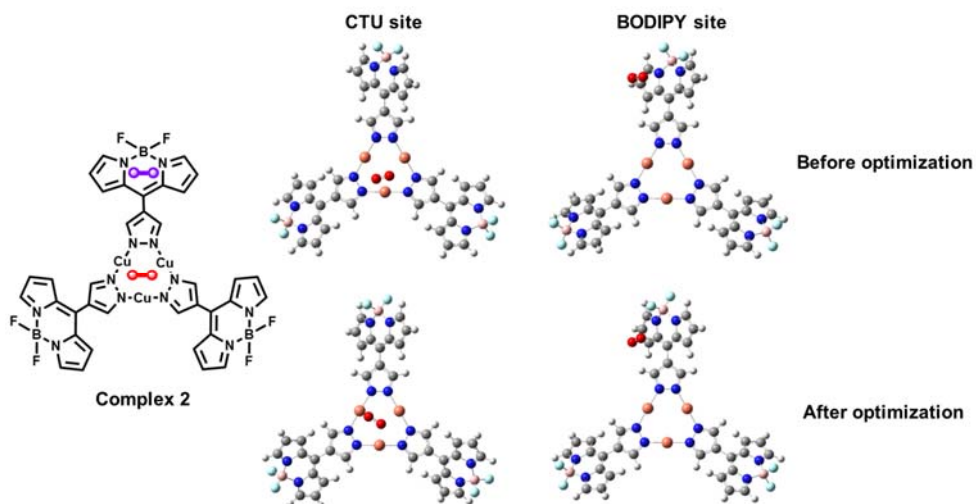
Fig. S57 The adsorption of O_2 on the BODIPY site and Cu_3N_6 site of **2**.
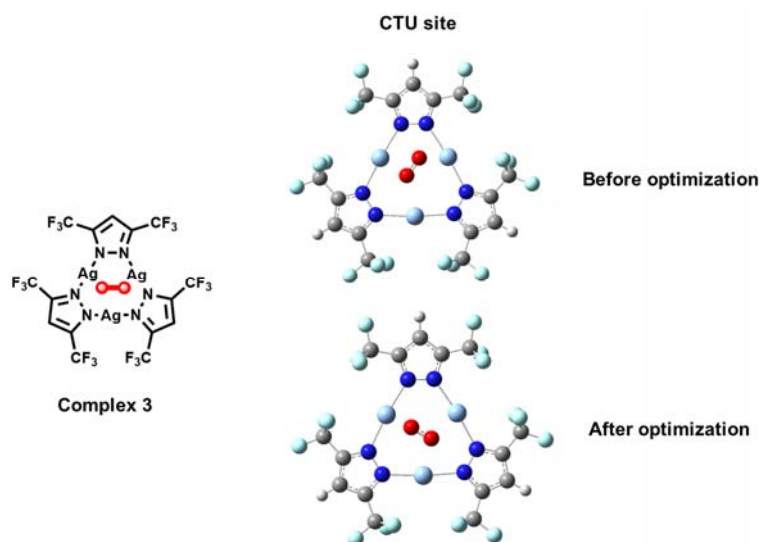
Fig. S58 The adsorption of O_2 on Ag_3N_6 site of **3**.

Table S5 The calculated adsorption free energies (eV) of O_2 at different active sites of **HL**, **1**, **2** and **3**.

Complex / Adsorption Site	HL	1	2	3
BODIPY site	0.1604	0.2469	0.2709	—
M_3N_6 site (M = Ag for **1**, and **3**; Cu for **2**)	—	0.1329	0.1732	0.1151
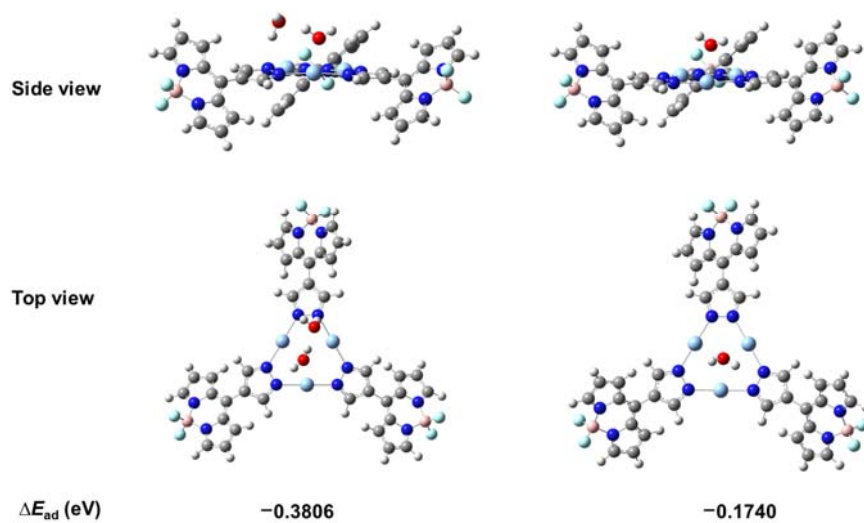
Fig. S59 Adsorption energies of H_2O on Ag_3N_6 site of **1**. Two H_2O molecules were adsorbed on Ag_3N_6 site (left), and one H_2O molecule was adsorbed on Ag_3N_6 site (left).
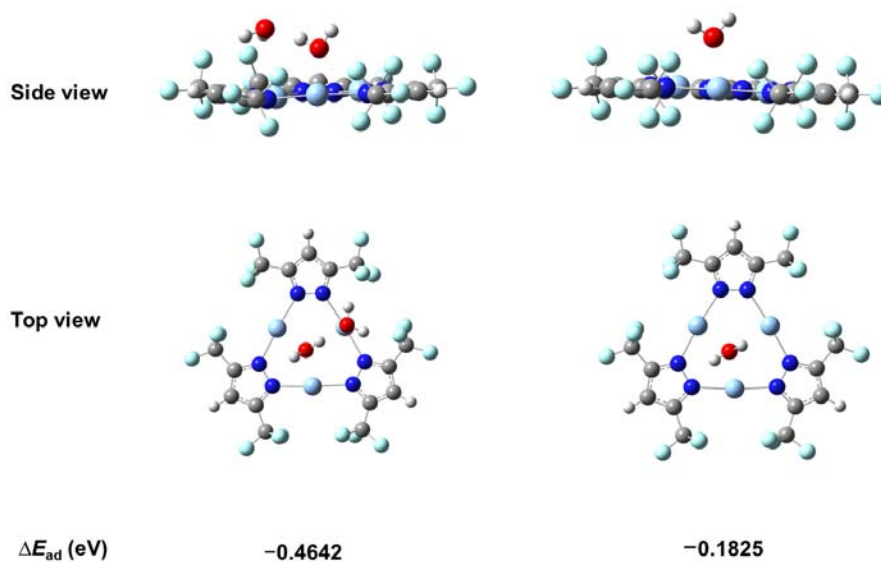
Fig. S60 Adsorption energies of H_2O on Ag_3N_6 site of **3**. Two H_2O molecules were adsorbed on Ag_3N_6 site (left), and one H_2O molecule was adsorbed on Ag_3N_6 site (left).

3.3 Reaction Gibbs Free Energy (ΔG)

The reaction Gibbs free energy was calculated the following equation[18]:

$$\Delta G = G(products) - G(reactants) \qquad (2)$$

The Gaussian software works by calculating the corrections to the enthalpy and entropy of formation or reaction based on total energy and contributions from vibrational, rotation, translational, or electronic motion. Thus, the reaction Gibbs free energy based on Gaussian was calculated in the following equation[19]:

$$\Delta rG = \sum(\varepsilon_0 + G_{Corr})products - \sum(\varepsilon_0 + G_{Corr})reactants \qquad (3)$$

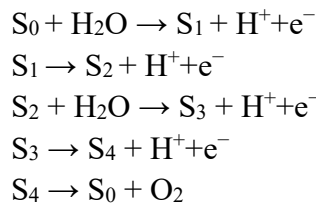The values of ε_0, G_{Corr} are calculated from the thermochemistry of H_2O_2 at the DFT level using B3LYP with a 6-31G(d,p) basis set, where ε_0 is the electronic energy, G_{Corr} is the Gibbs free energy correction. The sum of the electronic and Gibbs free energy and the sum of the electronic is used as $\varepsilon_0 + G_{Corr}$.

The free energy of $(H^+ + e^-)$ is considered by employing the computational hydrogen electrode model as proposed by Nørskov et al.[20] "$H^+ + e^-$" was assumed to be in equilibrium with $1/2\ H_2$, at pH = 0 and 0 V potential in SHE.[21]

For the O_2 production process, H_2O molecules are absorbed on the surface of photocatalysts, and adsorption free energy ΔE_{ad} was used to estimate the strength of adsorption. the OER process involves a four-electron reaction that sequentially forms *OH, *O, and *OOH or *O*OH intermediates. since the adsorption energy of the intermediate *OOH is lower than that of the intermediate *O*OH, here the preferable OER process is a single-site process which is summarized as below:

$$S_0 + H_2O \rightarrow S_1 + H^+ + e^-$$
$$S_1 \rightarrow S_2 + H^+ + e^-$$
$$S_2 + H_2O \rightarrow S_3 + H^+ + e^-$$
$$S_3 \rightarrow S_4 + H^+ + e^-$$
$$S_4 \rightarrow S_0 + O_2$$

where the asterisk (*) refers to the catalyst and active adsorption site on the catalyst. Where S_0 denotes the bare surface, S_1, S_2, S_3, and S_4 denote the intermediates of *OH, *O, *OOH, and *O_2 on reaction site. If the ΔG value of all the four elementary steps is different, the overpotential (η) used to further rationalize the catalytic performance of OER and would be calculated by using the following equations:

$$\eta^{OER} = \max\{\Delta G_a, \Delta G_b, \Delta G_c, \Delta G_d\} / e - 1.23 \qquad (4)$$
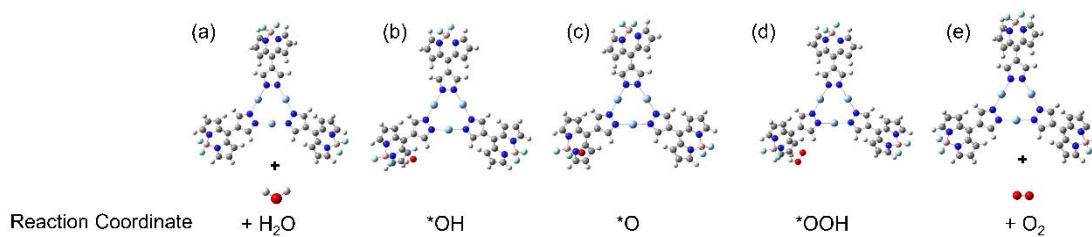
Fig. S61 The optimized geometries of reaction intermediates at the Ag_3N_6 site of **1**.
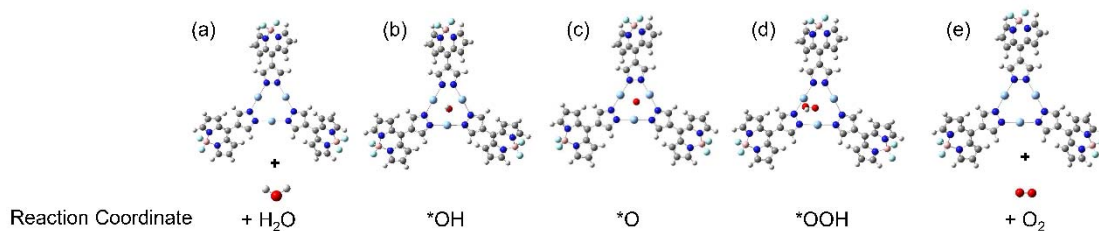
Fig. S62 The optimized geometries of reaction intermediates at the BODIPY site of **1**.
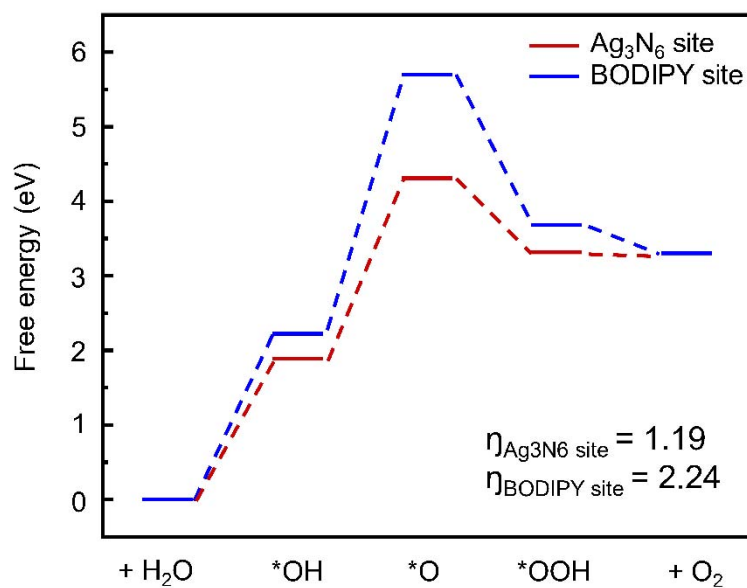
Fig. S63 Calculated free energy diagrams and overpotentials of four-electron water oxidation pathway on different active sites (bule line: BODIPY site, red line: Ag_3N_6 site)
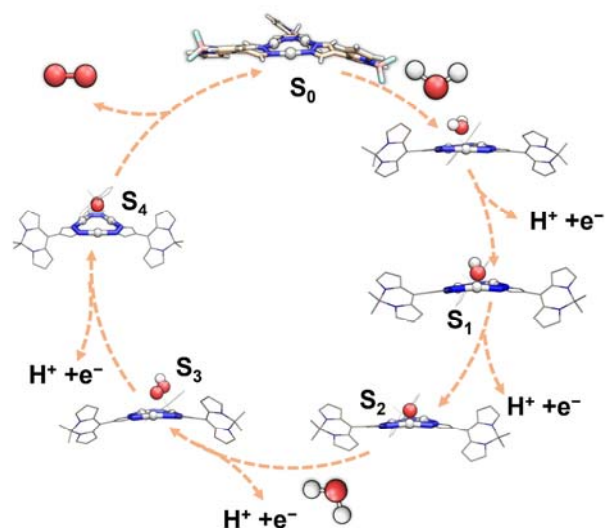
Fig. S64 The photocatalytic water oxidation reaction into O_2 production via a single-site process of **1**. S_0 is the bare surface and S_1-S_4 are the structures of intermediate states (*OH, *O, *OOH, *O_2) involved in the four-electron water oxidation process. The calculations are based on the Ag_3N_6 site.

Table S6 Photocatalytic H_2O_2 production performance of various reported noncovalent organic molecular assemblies. Note that the H_2O_2 production rate can depend strongly on the irradiation source and the precise experimental set-up, and hence these values can only be compared in a qualitative sense.

| Materials	The H_2O_2 production rate ($\mu M\ h^{-1}$)	Reference
Ag-CTC **1**	183.7 and 192.3 ($\lambda > 420$ nm) 298.6 ($\lambda > 420$ nm) with SA	This work
$[Ru^{II}(Me_2phen)_3]SO_4$	30 ($\lambda > 420$ nm) with WOC and Sc^{3+}	*J. Mater. Chem. A,* 2015, **3**, 12404–12412
$Ni^{II}[Ru^{II}(CN)_4(bpy)]$	34 ($\lambda > 390$ nm) with Sc^{3+} and SA	*Chem. Commun.,* 2017, **53**, 3473–3476
$[Fe(H_2O)_3]_2[Ru(CN)_6]@sAlMCM-41$	44 with Sc^{3+}	*Inorg. Chem.,* 2016, **55**, 5780−5786
ZnPPc-NBCN-1.5	57	*PNAS,* 2021, **118**, e2103964118
$[Ru^{II}(Me_2phen)_3]SO_4$	58 with WOC and Sc^{3+}	*Catal. Sci. Technol.,* **2016**, 6, 681–684
$[Ru^{II}(Me_2phen)_3]SO_4$	68 ($\lambda > 420$ nm) with WOC, P and Sc^{3+}	*Energy Environ. Sci.,* 2013, **6**, 3756–3764
$[Ir^{III}(Cp^*)(4-(1H-pyrazol-1-yl-\kappa N_2)benzoic\ acid-\kappa C_3)-(H_2O)]_2SO_4$	81 with NADH	*Inorg. Chem.,* 2016, **55**, 7747–7754
$[Ru^{II}((MeO)_2bpy)_3]SO_4$	114 with $BiVO_4$ and Sc^{3+}	*RSC Adv.,* 2016, **6**, 42041–420044
$(Cu(acac)_2/ms-BiVO_4)$	68 283 with SA	*J. Phys. Chem. C,* 2020, **124**, 3715–3721

SA: sacrificial reagent, WOC: water oxidation catalyst, P: proton source (e.g., H_2SO_4), NADH: 1,4-dihydronicotinamide adenine dinucleotide

Reference

1 Wei, Z.; Liu, M.; Zhang, Z.; Yao, W.; Tan, H.; Zhu, Y., *Energy Environ.Sci.,* 2018, **11**, 2581–2589.

2 Lingampalli, S.; Gautam, U. K.; Rao, C., *Energy Environ. Sci.,* **2013**, 6, 3589–3594.

3 Xia, R.-Q.; Zheng, J.; Wei, R.-J.; He, J.; Ye, D.-Q.; Ning, G.-H.; Li, D., *Inorg. Chem. Front.,* 2022, **9**, 2928–2937.

4 Sheldrick, G., *Acta Cryst. A,* 2008, **64**, 112–122.

5 Dolomanov, O. V.; Bourhis, L. J.; Gildea, R. J.; Howard, J. A. K.; Puschmann, H., OLEX2: *J. Appl. Cryst.,* 2009, **42**, 339–341.

6 Li, X.; Kang, B.; Dong, F.; Zhang, Z.; Luo, X.; Han, L.; Huang, J.; Feng, Z.; Chen, Z.; Xu, J.; Peng, B.; Wang, Z. L., *Nano Energy,* 2021, **81**, 105671.

7 Frisch, M.; Trucks, G.; Schlegel, H.; Scuseria, G.; Robb, M.; Cheeseman, J.; Scalmani, G.; Barone, V.; Mennucci, B.; Petersson, G. Fox. Gaussian 09 (Revision E. 01). Gaussian. Inc., *Wallingford, CT,* 2009.

8 S. Grimme, J. Antony, S. Ehrlich and H. Krieg, *J. Chem. Phys.,* 2010, **132**, 154104.

9 S. Grimme, S. Ehrlich and L. Goerigk, *J. Comput. Chem.,* 2011, **32**, 1456–1465.

10 T. H. Dunning, Jr., and P. J. Hay, In Modern Theoretical Chemistry; Schaefer, H. F., III., *Ed. Plenum: New York,* 1976, **3**, 1–28.

11 P. J. Hay and W. R.Wadt., *J. Chem. Phys.,* 1985, **82**, 270.

12 W. R.Wadt and P. J. Hay, *J. Chem. Phys.,* 1985, **82**, 284.

13 P. J. Hay and W. R.Wadt, *J. Chem. Phys.,* 1985, **82**, 299.

14 P. C. Hariharan, and J. A. Pople, A. *Mol. Phys.,* 1974, **27**, 209.

15 T. Lu and F. Chen, *J. Comput. Chem.,* 2012, **33**, 580–592.

16 Z. Liu, T. Lu, Q. Chen, *Carbon,* 2020, **165**, 461–467.

17 Karlberg, G. S.; Jaramillo, T. F.; Skúlason, E.; Rossmeisl, J.; Bligaard, T.; Nørskov, J. K., *Phys. Rev. Lett.,* 2007, **99**, 126101.

18 Ochterski J W. *Gaussian Inc,* 2000, **1**, 1–20.

19 Pintea M, Mason N, Peiró-Franch A, et al. *Front. Chem.,* 2023, **11**, 1028008.

20 Nørskov, J. K.; Rossmeisl, J.; Logadottir, A.; Lindqvist, L.; Kitchin, J. R.; Bligaard, T.; Jonsson, H., *J. Phys. Chem. B,* 2004, **108**, 17886–17892.

21 Han, G.; Zhang, X.; Liu, W.; Zhang, Q.; Wang, Z.; Cheng, J.; Yao, T.; Gu, L.; Du, C.; Gao, Y.; Yin, G., *Nat. Commun.,* 2021, **12**, 6335.